

VICTOR HUGO BENEZOLI

**MODELING OF OIL PALM ENERGY SURFACE FLUXES AND GROWTH FOR
BRAZILIAN AMAZON CLIMATE CONDITIONS**

Thesis submitted to the Applied Meteorology
Graduate Program of the Universidade Federal de
Viçosa in partial fulfillment of the requirements
for the degree of *Doctor Scientiae*.

Adviser: Hewlley Maria Acioli Imbuzeiro

Co-advisers: Santiago Vianna Cuadra

**VIÇOSA - MINAS GERAIS
2020**

**Ficha catalográfica elaborada pela Biblioteca Central da Universidade
Federal de Viçosa - Campus Viçosa**

T

B435m
2020

Benezoli, Victor Hugo, 1988-

Modeling of oil palm energy surface fluxes and growth for
Brazilian Amazon climate conditions / Victor Hugo Benezoli. –
Viçosa, MG, 2020.

55 f. : il. (algumas color.) ; 29 cm.

Orientador: Hewlley Maria Acioli Imbuzeiro.

Tese (doutorado) - Universidade Federal de Viçosa.

Referências bibliográficas: f.52-55.

1. Palmeira oleaginosa - Cultivo - Amazônia.

2. Climatologia agrícola. 3. ECOSMOS (Modelo agroclimático).

I. Universidade Federal de Viçosa. Departamento de Engenharia
Agrícola. Programa de Pós-Graduação em Meteorologia
Aplicada. II. Título.

CDD 22. ed. 633.851

VICTOR HUGO BENEZOLI

**MODELING OF OIL PALM ENERGY SURFACE FLUXES AND GROWTH FOR
BRAZILIAN AMAZON CLIMATE CONDITIONS**

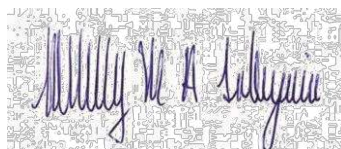
Thesis submitted to the Applied Meteorology
Graduate Program of the Universidade Federal de
Viçosa in partial fulfillment of the requirements
for the degree of *Doctor Scientiae*.

APPROVED: August 12, 2020.

Assent:



Victor Hugo Benezoli
Author



Hewlley Maria Acioli Imbuzeiro
Adviser

To my parents.

ACKNOWLEDGEMENTS

First of all, I would like to thank God for my life and for making me able to conduct this study.

I also want to thank my parents José Benezoli and Eliana Barcelos Benezoli and my sister Marcela Benezoli for supporting me at all times, so that without them none of this would have been possible.

I also thank my fiancée Gabriela Lovato for the support and affection at all times and for encouraging me to continue to pursue my goals.

I am grateful to my friends, especially colleagues from the Research Group on Atmosphere-Biosphere Interactions, mainly Ana Beatriz Santos, Raphael Pousa, Gabriel Abrahão, Emily Silva, Vitor Fontes, and Matheus Lucas, who helped me carry out this study. I also want to thank my friends from the MICROMET group, Gabriel Peterle, Heitor Filpi, Sandro Silva, Gisele Almeida, and Bruna Paim for their support at all times and for their contribution to this study. I also thank all of these friends for the many fun moments we had together.

I thank the Universidade Federal de Viçosa (UFV) for contributing to my intellectual and personal growth. When I see my entire journey here, I am proud to have been part of UFV.

I would like to thank all the employees of the Agricultural Engineering Department, especially Graça Freitas, who undoubtedly contributed to what my graduate studies went through in the best possible way.

I also want to thank my advisors Hewlley Imbuzeiro and Santiago Cuadra for all their support and guidance. This study would not be possible without the collaboration of both.

Finally, I also thank CAPES for the financial support granted through the scholarship. This study was financed in part by the *Coordenação de Aperfeiçoamento de Pessoal de Nível Superior – Brasil* (CAPES) – Finance Code 88882.437129/2019-01. I also thank Agropalma for the financial and technical support and for the data made available for this study, and Embrapa Amazônia Oriental and Marborges Agroindustry for the micrometeorological data used in this study.

*“Imagination will often carry us to worlds that never
were. But without it we go nowhere.”.*
(Carl Sagan)

ABSTRACT

BENEZOLI, Victor Hugo, D.Sc., Universidade Federal de Viçosa, August 2020. **Modeling of oil palm energy surface fluxes and growth for Brazilian Amazon climate conditions.** Adviser: Hewlley Maria Acioli Imbuzeiro. Co-adviser: Santiago Vianna Cuadra.

The increase in demand for African palm oil (*Elaeis guineensis* Jacq.) has caused an increase in production, especially through the opening of new areas. Due to the limitation of lands in Southeast Asia, which is the main producing region in the world, the expansion of oil palm plantation has occurred in Latin American countries, such as Brazil. Roughly 400 million hectares in Brazil are suitable for the planting of oil palm, but half of this is currently covered by forest, mainly by the Amazon Rainforest. Also, climate change has reduced the amount of land suitable for oil palm plantation in Brazil, since, under unfavorable climatic conditions, crop yield is reduced. To reconcile the increase in oil palm production in Brazil with the conservation of forests, modeling has been used widely as a tool to define the best suitable areas for planting expansion, as well as for the assessment of management techniques that aim to increase the yield. Thus, the aim of this study was to implement the oil palm crop in the ECOSMOS model and to evaluate the model's ability to simulate the energy and carbon balance, as well as the crop yield. The carbon allocation scheme for oil palm is quite different from the other crops implemented in ECOSMOS. Thus, we use the sub-PFT approach, so that each phytomer in the plant evolves simultaneously, but individually. The results showed that the model was able to simulate with good accuracy the net radiation (R_n), the latent heat flux (LE), and the net ecosystem CO_2 exchange (NEE), but it was not able to simulate with satisfactory accuracy the sensible heat flux (H) due to the lack of information on the soil physical-hydric properties. In addition, the model was able to accurately simulate the annual yield for plants aged between 12 and 25 years. For plants aged outside this range, the yield was overestimated. Besides, the model was able to better simulate genetic varieties that show seasonality in yield. However, despite presenting good results to simulate the energy and carbon flux, as well as the crop yield, the model still needs to consider key factors for oil palm, such as the ratio between male and female inflorescences and the abortion rate of inflorescences, which affect crop yield.

Keywords: Amazon. Agriculture. ECOSMOS.

RESUMO

BENEZOLI, Victor Hugo, D.Sc., Universidade Federal de Viçosa, agosto de 2020. **Modelagem dos fluxos superficiais de energia e do crescimento da palma de óleo para condições climáticas da Amazônia brasileira.** Orientador: Hewlley Maria Acioli Imbuzeiro. Coorientador: Santiago Vianna Cuadra.

O aumento da demanda mundial pelo óleo da palma africano (*Elaeis guineensis* Jacq.) tem causado aumento na produção, principalmente através da abertura de novas áreas. Devido à limitação de terras no sudeste da Ásia, que é a principal região produtora do mundo, a expansão da área plantada de palma de óleo vem ocorrendo em países da América Latina, como o Brasil. Aproximadamente 400 milhões de hectares no Brasil são adequados para o plantio de palma de óleo, mas metade disso é atualmente coberta por florestas, principalmente pela Floresta Amazônica. Além disso, as mudanças climáticas podem reduzir a quantidade de terras adequadas para o plantio de palma de óleo no Brasil, uma vez que, em condições climáticas desfavoráveis, a produtividade diminui. Para conciliar o aumento da produção de palma de óleo no Brasil com a manutenção das florestas, a modelagem tem sido amplamente utilizada como ferramenta para definir as áreas mais adequadas para expansão do plantio, bem como para a avaliação de técnicas de manejo que visam aumentar o rendimento. Assim, o objetivo deste estudo foi implementar a cultura da palma de óleo no modelo ECOSMOS e avaliar a capacidade do modelo em simular o balanço de energia e de carbono, bem como a produtividade da cultura. O esquema de alocação de carbono para a palma de óleo é bem diferente das outras culturas implementadas no ECOSMOS. Assim, usamos a abordagem sub-PFT, de forma que cada fitômero na planta evolui simultaneamente, mas individualmente. Os resultados mostraram que o modelo foi capaz de simular com boa precisão o saldo de radiação (R_n), o fluxo de calor latente (LE) e a troca líquida de CO_2 no ecossistema (NEE), mas não foi capaz de simular com precisão satisfatória o fluxo de calor sensível (H) devido à falta de informações sobre as propriedades físico-hídricas do solo. Além disso, o modelo foi capaz de simular com precisão a produtividade anual para plantas com idades entre 12 e 25 anos. Para plantas fora dessa faixa, a produtividade foi superestimada. Além disso, o modelo foi capaz de simular melhor as variedades genéticas que mostram sazonalidade na produtividade. No entanto, apesar de apresentar bons resultados para simular o fluxo de energia e carbono, bem como a produtividade da cultura, o modelo ainda precisa considerar processos importantes para a palma de óleo, como a razão sexual e a taxa de aborto de inflorescências, que afetam a produtividade da cultura.

Palavras-chave: Amazônia. Agricultura. ECOSMOS.

LIST OF ILLUSTRATIONS

Figure 1 – Maps of the region of study located in Brazil (a) and Indonesia (b).....	20
Figure 2 – Diagram of the sensitivity analysis and model calibration.	25
Figure 3 – List of parameters whose model shown to be sensitive to simulate H, LE, and NEE. Black circles represent the p-value of the parameter coefficients of the linear regression fitted between the MAE of the simulations and the values of the parameters. The dashed red line represents the 90% probability threshold for considering that the model was sensitive to the parameter to simulate H, LE, and NEE	28
Figure 4 – Coefficient of variation (CV) of the parameters that performed the 5% best simulation results for H, LE, and NEE.....	30
Figure 5 - Behavior of (a) evapotranspiration (ET) in relation to the variation of the vapor pressure deficit (VPD) and the net ecosystem productivity (NEE) variation during the day (b) and at night (c) in relation to the air temperature. The red and blue circles correspond to the measured and simulated data, respectively.....	32
Figure 6 – Linear regression fitted between observed and simulated net radiation (a), and the simulated (blue line) and observed (red line) net radiation diurnal cycle (b). R^2 is the coefficient of determination.....	33
Figure 7 - Linear regression fitted between observed and simulated latent heat flux (a), and the simulated (blue line) and observed (red line) latent heat flux diurnal cycle (b). R^2 is the coefficient of determination.....	34
Figure 8 - Linear regression fitted between observed and simulated sensible heat flux (a), and the simulated (blue line) and observed (red line) sensible heat flux diurnal cycle (b). R^2 is the coefficient of determination.....	35
Figure 9 - Linear regression fitted between observed and simulated net CO ₂ ecosystem exchange (a), and the simulated (blue line) and observed (red line) net CO ₂ ecosystem exchange diurnal cycle (b). R^2 is the coefficient of determination.....	35
Figure 10 - Distribution of the NEE bias (%) according to the friction velocity (u^* ; m s ⁻¹) and according to the frequency (a and b, respectively). Light red present the daytime NEE bias and the light blue is the nighttime NEE bias in both frames.....	36
Figure 11 – Daytime average of WUE (a) and LUE (b) for the MOJ site. The circles and lines in red represent the measured values, while the circles and lines in blue show the results of the simulation	37
Figure 12 - Monthly daytime of (a) water use efficiency (WUE) and (b) light use efficiency (LUE) in 2015 for MOJ site. Solid and dashed lines show the observed and simulated values from both WUE and LUE, respectively	38
Figure 13 - Water and light use efficiencies variation in relation with air temperature (a and c) and vapor pressure deficit (b and d). Solid and dashed line presented the exponential decay curve for observed and simulated data, respectively	39

Figure 14 - Decomposition of WUE into NEP and ET components. Iso-efficiency is shown by black dashed lines with their respective values of WUE. Circle colors present the VPD (a) and air temperature (b)	39
Figure 15 - Decomposition of LUE into NEP and PAR components. Iso-efficiency is shown by black dashed lines with their respective values of LUE. Circle colors present the VPD (a) and air temperature (b)	40
Figure 16 – Oil palm average yield according to the plantation age. Light red and blue bars are the observed and simulated monthly yield, and the vertical lines are the standard deviation ..	41
Figure 17 - Average monthly yield for each plot groups. The letters A to G are the centroid of the farms. There is no data for farm F	42
Figure 18 – Monthly yield bias distribution for each farm (left-side frame). Bars show the median \pm standard deviation. The color of the circles is the plant age when the yield was simulated. Boxplot in the right-side frame present the distribution of the RB of the plot groups in the farms, so that the box includes 50% of the data, with the horizontal tick inside the box as the median. Black dots represent the RB of each farm	43
Figure 19 – Yield monthly mean for farms A, B, C, D, E, G, and H. Light red bars present the observed yield data and blue bars present the simulated yield.....	44
Figure 20 – Seasonal yield behavior of the five most planted varieties in the study area. Deli x La Mé is the most planted variety in the study area (27%), followed by Deli x Ghana (14%), Deli x Ekona (12%), Deli x Avros (10%), and Deli x Nigeria (9.5%). Light red and blue lines present the observed and simulated monthly mean yield, respectively.....	45

LIST OF TABLES

Table 1 – Climate dataset availability for the weather station placed in the studied sites.	22
Table 2 – List of varieties per farm. The superscripts represent the proportion of the variety in the farm, where *** $\geq 50\%$, ** $\geq 25\%$, * $\geq 10\%$, and FS (few samples) $\geq 5\%$. Less than 5% is not shown. The variety names are according to the provided database	23
Table 3 – Summary of parameter values calibrated to simulate H, LE, and NEE	31

LIST OF ACRONYMS AND ABBREVIATIONS

CV	Coefficient of Variation
ET	Evapotranspiration
FFB	Fresh Fruit Bunches
G	Ground heat flux
H	Sensible heat flux
LAI	Leaf Area Index
LE	Latent heat flux
LUE	Light Use Efficiency
MAE	Mean Absolute Error
NASA	National Aeronautics and Space Administration
NEE	Net Ecosystem exchange
NEP	Net Ecosystem Production
NPP	Net Primary Production
PAR	Photosynthetically Active Radiation
PFT	Plant Functional Type
PPFD	Photosynthetic Photon Fluence Density
RB	Relative Bias
T	Air temperature
USDA	United States Department of Agriculture
VPD	Vapor Pressure Deficit
WUE	Water Use Efficiency
YPP	Years Past Planting

SUMMARY

1. INTRODUCTION	13
2. MATERIAL AND METHODS	16
2.1. The ECOSMOS-Palm model	16
2.1.1. Phenology and carbon allocation	18
2.2. Region of study and experimental field data	19
2.2.1. Region of study	19
2.2.2. Eddy covariance measurements	21
2.2.3. Climate data	21
2.2.4. Yield data	23
2.2.5. Soil properties	23
2.3. Model calibration and validation strategies	24
2.3.1. Sensitive analysis and calibration	24
2.3.2. Model validation	25
2.4. Oil palm carbon uptake and assimilation	26
2.5. Yield simulations	27
3. RESULTS	28
3.1. Sensitivity analysis and calibration	28
3.2. Energy and carbon fluxes simulation	32
3.2.1. Model validation	32
3.2.1.1. Oil palm carbon uptake and assimilation	36
3.3. Yield simulations	40
4. DISCUSSION	47
4.1. Climate dependence on oil palm carbon uptake efficiency	47
4.2. Modelling the oil palm growing and yield	48
5. CONCLUSIONS	51
6. REFERENCES	52

1. INTRODUCTION

The oil of African palm (*Elaeis guineensis* Jacq.) is the vegetable oil with the highest production and commercialization volume in the world. According to the United States Department of Agriculture (USDA), the global production in 2019 was 75.19 million tons of processed oil, higher than the production of soy oil in the same period (56.86 million tons). The oil extracted from the palm fruit has several uses in the industry, such as in food, in the composition of detergents and cosmetics, and more recently in the production of biodiesel (Pirker *et al.*, 2016). Most of the world's production comes from Southeast Asia. According to USDA, Indonesia is the main world producer, with 57.19% of the world production, followed by Malaysia (27.26%) and Thailand (3.99%). Together, the three countries produce almost 90% of the total of palm oil in the world.

The demand for palm oil has caused an increase in production. Currently, the world production has doubled since 2005, from 36 million tons of processed oil to the current 72 million, according to USDA. However, much of this increase in production was a result of the increase in planted area, and not an increase of yield (Furumo and Aide, 2017). The planted area of oil palm has doubled since 2003, from 11.7 million hectares to the current 23.7 million hectares. In addition, the ideal oil palm production conditions are on tropical forest areas. According to Furumo and Aide (2017), more than half of the new palm planted areas came from tropical forest in Malaysia and Indonesia during 1990-2005 period. Worldwide, oil palm cultivation was accountable for the conversion of 270,000 ha per year of forests in cultivated areas between the years 2000 and 2011 (Vijay *et al.*, 2016).

Latin America has emerged as a feasible alternative to Southeast Asia to increase world palm oil production. Currently, Colombia is the main producer of palm oil in Latin America and the fourth largest producer in the world. Brazil has a small contribution to the international market, ranking ninth and accounting for 0.72% of world production. However, the modest Brazilian oil palm production has been expanding. According to USDA, national production increased from 2.7 million tons in 2010 to 5.4 million tons in 2019. This expansion is linked both to the creation of incentive governmental programs to increase the palm oil production, such as Pronaf Eco Dendê (Monteiro de Carvalho *et al.*, 2015), as well as the increase in domestic and international demand. The Pará state is the largest producer of palm oil in Brazil, accounting for 70% of the total planted area and 90% of national production.

Oil palm tree is a plant that is a member of the *Arecaceae* family. An important characteristic of the plants of this family is the presence of a single apical vegetative meristem

that gives rise to the phytomers (the leaf and the underlying fruit bunch) in regular succession (Adam *et al.*, 2005). Each phytomer supports a large leaf and an inflorescence structure in the axil that could be male or female. After reaching maturity, each plant is able to produce one phytomer every 15-18 days on average, depending on environmental and endogenous factors, such as water stress, air temperature, number of female inflorescences, and age (Breure, 1994; Woittiez *et al.*, 2017). So, the plant is able to produce bunches of fruits and keeps vegetative growth at the same time throughout life (Forero, Hormaza and Romero, 2012).

Oil palm emerged in the tropical forests of western and central Africa, with its center of diversity possibly located in Nigeria (Hayati *et al.*, 2004; Maizura *et al.*, 2006). The climate in this region is rainy, warm, and humid, so that the demand for water and temperature by plant is high. Corley and Tinker (2015) estimate that the plant grows well in regions with well distributed annual rainfall above 2,000 mm, mean air temperature between 24°C and 28°C, and relative humidity higher than 85%.

The most suitable areas for oil palm plantations in the world are in equatorial regions, such as Southeast Asia, Sub-Saharan Africa and South and Central America. In Brazil, more than 400 million ha are suitable for the cultivation of oil palm, but almost half of this area is currently covered by tropical forests, especially in the Amazon region (Pirker *et al.*, 2016; Vijay *et al.*, 2016). Furthermore, a large part of this area is under threat of becoming unsuitable for oil palm production. Almeida *et al.* (2017) reported that most of the Amazon region has been experiencing a consistent increase in the mean air temperature since the 1970s, including the eastern Amazon, where the main Brazilian oil palm plantations are placed. Da Silva *et al.* (2019) reported an increase in the frequency of extreme temperature and precipitation events in eastern Amazonia, which include heat waves, warmer days and cooler nights, as well as a drier climate with poorly distributed rainfall. Furthermore, Avila-Diaz *et al.* (2020) pointed out that these trends of extreme temperature and precipitation events in eastern Amazonia will be remaining in the future. These climate conditions could result in a substantial reduction in suitable areas to oil palm production in Brazil, as suggested by Paterson *et al.* (2017), and also reducing yield in current suitable areas. In addition, due to the Amazon Rainforest currently covers most of the areas suitable for oil palm cultivation in Brazil, the expansion of Brazilian oil palm plantations may lead to an undesirable increase in deforestation in the Amazon.

The challenges imposed to the growth of oil palm production in Brazil due to competition by area with the Amazon Rainforest and climate change require a deepening of knowledge about the plant's life cycle, including growth and yield. Previous studies have shown

how the environment and endogenous factors of the plant, such as age and reproductive cycle, affect the growth and yield of oil palm (Hoffmann *et al.*, 2017; Woittiez *et al.*, 2017). However, it is still unclear how large the contribution of each climate factor is to carbon uptake and assimilation in oil palm. Furthermore, it is necessary to understand how these climatic factors affect the crop yield. A tool widely used in studies involving the relationship between agricultural production and the climate is the land surfaces model. These models are able to simulate crop yields under different climatic conditions, explicitly simulating processes such as photosynthesis, respiration, and phenology, as well as the exchange of carbon, water and energy between the biosphere and the atmosphere (Sellers, 1997). In addition, modeling allows to assess the impact of management techniques on carbon assimilation and yield, as well as assessing the suitability of areas for the cultivation of different agricultural species, avoiding the deforestation of low-yield areas.

There are currently several models that simulate oil palm yield, such as APSIM-Palm (Huth *et al.*, 2014), ECOPALM (Combres *et al.*, 2013), PALMSIM (Hoffmann *et al.*, 2014), and CLM-Palm (Fan *et al.*, 2015). However, most of these models simplify land surface processes and limit assimilation to a few climatic factors, such as solar radiation and soil water content. Few models, such as CLM-Palm, are able to simulate growth, yield and exchanges of carbon, water and energy between the ecosystem and the atmosphere. In this study the ECOSMOS-Palm sub-model is presented, which simulates the growth and yield of oil palm through the structure of the ECOSMOS model, based on the Agro-IBIS model (Foley *et al.*, 1996; Kucharik and Brye, 2003). In addition, the sub-PFT scheme proposed by Fan *et al.* (2015) was used to implement phenology and carbon allocation to the plant pools (roots, trunk, leaves, and fruits).

Thus, the objectives of this study are (i) to implement the oil palm crop model in the ECOSMOS integrated simulator, (ii) to evaluate modelled crop carbon assimilation and energy balance through two micrometeorological flux tower measurements, and (iii) to investigate modelled crop yield response to climatic and meteorological conditions of the main producing region in Brazil.

2. MATERIAL AND METHODS

2.1. The ECOSMOS-Palm model

ECOSMOS is a biophysical growth model based on Agro-IBIS (Foley *et al.*, 1996; Kucharik and Brye, 2003). Researchers from EMBRAPA (Brazilian Agricultural Research Company) have re-written the Agro-IBIS code in the R and C++ languages, and have been implementing the most common crops in Brazil. One of the major changes in the ECOSMOS framework is that developers can add new Crops-PFT (plant functional type) as module in R, and this crop module is linked with the core model sub-routines that solves the biophysical processes, such as photosynthesis, energy balance, and soil water dynamics.

Like Agro-IBIS model, the ECOSMOS structure is divided into four main modules: (i) land surface processes module; (ii) crop dynamics module; (iii) belowground carbon and nitrogen cycle module; and (iv) crop phenology module (Kucharik and Brye, 2003). The land surface processes module simulates on a 60-minute timescale both canopy and soil physics in addition to plant physiology (photosynthesis, leaf respiration, and stomatal conductance). The crop dynamics module simulates both the gross and net primary production (GPP and NPP, respectively) and total ecosystem respiration on a daily to annual timescale. Belowground carbon and nitrogen cycle module simulate the soil respiration, litter decomposition, and nitrogen cycle processes such as nitrogen mineralization, fixation, and deposition, fertilization, and plant uptake also on a daily to annual timescale. Last, the phenology module simulates on a daily timescale the crop phenological processes based on the degrees-day method.

Regarding plant physiology, the simulation of photosynthesis and respiration are different for C₃ and C₄ plants. In C₃ plant, such as oil palm, the stomatal conductance is coupled to photosynthesis and regulates plant transpiration, according to Collatz *et al.* (1991) strategy. Stomatal conductance (g_s) simulation in ECOSMOS is affected by CO₂ and H₂O air concentration close to leaf surface, as well as by the current leaf photosynthesis rate, according to the Leuning (1995) formulation, as follows:

$$g_s = m \frac{A_n}{(C_s - \Gamma_*) \left(\frac{D_s}{D_o} \right)} + b \quad \text{Eq. 1}$$

where m and b are empirical plant-specific parameters, C_s is the CO₂ mole fraction, D_s is the water vapor deficit, D_o is a reference value, Γ_* is the CO₂ compensation point, and A_n is the current net photosynthesis rate. Net photosynthesis rate simulation, in turn, is limited by light, temperature, and CO₂ concentration (Farquhar, von Caemmerer, and Berry, 1980), as follows:

$$A_n = \min(J_E, J_C, J_S) - R_d \quad \text{Eq. 2}$$

where J_E , J_C , and J_S describe the photosynthetic rates limited by light, ribulose biphosphate carboxylase (Rubisco), and sucrose synthesis capacity, respectively, and R_d is the daytime respiration rate (Collatz *et al.*, 1991). In other words, net photosynthesis rate is equal to the most limiting assimilation rate. Note that the photosynthetic rate is dependent on climatic conditions, since it can be limited by solar radiation, by temperature (which affects the CO_2 fixation capacity of the Rubisco enzyme, V_{\max}), or even by the atmospheric humidity, which affects stomatal conductance.

The oil palm is an evergreen perennial crop, setting it apart from other crops existing in the ECOSMOS model. The life cycle of the oil palm in the model starts with the transplanting of the seedling. The plant does not produce fruit bunches in the first 2-3 years (vegetative growing stage), but in the mature stage, it usually can produce fruit bunches for at least 25 years. During the vegetative growing stage, the plant allocates NPP only to the vegetative growth pools.

Phenology and carbon allocation schemes was based on the sub-canopy structure developed by Fan *et al.* (2015). The phenology of the phytomers evolves simultaneously, but independently. Each phytomer works as a sub-PFT evolving in a sequential order controlled by the phyllochron (the thermal time necessary to start a phytomer) in which the newer, tinier phytomers overlap the older, larger. Although the phenological evolution is individual, the phytomers share the same root system and the same single stem (Fan *et al.*, 2015).

The phytomer life cycle was divided into five stages in the model: (i) leaf spear (unopened leaf) initialization; (ii) leaf opening; (iii) leaf maturity; (iv) bunch fruit filling; and (v) leaf senescence. During the first stage, the leaf spears do not perform photosynthesis, so they do not contribute to the LAI (leaf area index). In the second stage, the plant gradually transfers the carbon allocated in the leaf spear pool to the opened, photosynthetically activated leaf pool. In the third stage, the leaf grows until reaching maturity. In the fourth stage, the plant allocates NPP to the fruit filling until the ripe, and then it is ready for harvest. Harvesting usually takes place once a month for management issues. Senescence is the last phase of the phytomer's life cycle. At this stage, the phytomer no longer receives carbon assimilated by the plant and begins to wilt. Finally, the leaf is pruned right after completing the senescence stage.

2.1.1. Phenology and carbon allocation

During the vegetative growing stage, all plant stocks all assimilated carbon in the vegetative structures (leaves, root system and stem), which means that the fourth leaf growth stage does not occur. The following allometric equations fractionate carbon into root (A_{root}), stem (A_{stem}), and leaf (A_{leaf}) pools during the vegetative growth stage.

$$A_{\text{root}} = a_{\text{root}}^i - (a_{\text{root}}^i - a_{\text{root}}^f) \frac{\text{DDP}}{A_{\text{max}}} \quad \text{Eq. 1}$$

$$A_{\text{leaf}} = a_{\text{leaf}}^i (1 - A_{\text{root}}) \quad \text{Eq. 2}$$

$$A_{\text{stem}} = 1 - A_{\text{root}} - A_{\text{leaf}} \quad \text{Eq. 3}$$

where a_{root}^i and a_{leaf}^i are the initial allocation coefficients for roots and leaves in the vegetative growing stage, and a_{root}^f is the final allocation coefficient for roots. DPP is the number of the days past since the plant was transplanted, and A_{max} is the maximum plantation age (in days). The stem allocation also was divided into live and dead (woody) pools by a stem coefficient.

During the productive stage, part of the carbon is allocated for the fruit filling. However, only phytomers that are in the fruit filling stage will receive carbon allocated to the fruits. The following equation presents the fraction of NPP that will be allocated to fruit filling (A_{fruit}).

$$A_{\text{fruit}} = \frac{2}{1 + e^{-b(\text{NPP}_{\text{mon}} - 100)}} - a \quad \text{Eq. 4}$$

where a and b are the adjustment coefficients that control the exponential equation (base value and shape, respectively), NPP_{mon} is the sum of NPP in the previous month, and the number 100 (in $\text{g-C m}^{-2} \text{ mon}^{-1}$) is the NPP of the month before oil palm reaches the productive stage (Kotowska *et al.*, 2015). A_{fruit} varies from 0 to 2 and it is relative to the vegetative unity, which means all vegetative fractions must be multiplied by a reduction factor (r_f). The fruit fraction (A_{fruit}) is now the difference between the sum of the reduced vegetative fractions and the unit.

$$r_f = \frac{1}{1 + A_{\text{fruit}}} \quad \text{Eq. 5}$$

$$A_{\text{fruit}} = 1 - r_f (A_{\text{root}} + A_{\text{leaf}} + A_{\text{stem}}) \quad \text{Eq. 6}$$

The leaf fraction allocation changes in the mature stage due to the change in the phytomer allocation strategy, according to the following equation:

$$A_{\text{leaf}} = a_{\text{leaf}}^p - (a_{\text{leaf}}^p - a_{\text{leaf}}^f) \times \left(\frac{\text{DPP} - \text{DPP}_2}{A_{\text{max}} \times d_{\text{mat}} - \text{DPP}_2} \right)^{d_{\text{alloc}}^{\text{leaf}}} \quad \text{Eq. 7}$$

where a_{leaf}^p is the leaf allocation fraction just before the productive stage starts, DPP_2 is the number of days until the productive stage starts, d_{mat} controls the stability of the non-linear curve based on the age of the plant, and $d_{\text{alloc}}^{\text{leaf}}$ controls the shape of the equation (convex or concave for negative or positive values, respectively).

The carbon allocation strategy within the sub-PFT structure depends on the phenological stage of each phytomer. For leaves, the total carbon fraction allocated is divided into leaf spears and opened leaves pools according to factor f_s (fraction allocated to the leaf spears pool). The carbon allocated for each pool is then divided by the same portion for each phytomer, except for those in senescence. Also, opened leaves receive gradually the carbon of the leaf spears that reaches the stage two of the phytomer life cycle. The fruit bunch accumulates carbon allocated for fruit filling at an increasing rate, where bunches of fruit close to ripening receive more carbon, according to the following equation.

$$S_p^{\text{fruit}} = \frac{\text{GDD}_{15} - \text{GDD}_{\text{min}}^{\text{fmat}}}{\text{GDD}_{\text{min}}^{\text{fmax}} - \text{GDD}_{\text{max}}^{\text{fmat}}} \quad \text{Eq. 8}$$

where S_p^{fruit} is the carbon sink size of phytomer p ($0 \leq S_p^{\text{fruit}} \leq 1$), GDD_{15} is the GDD with 15°C base temperature accumulated for each phytomer since the leaf opening, and $\text{GDD}_{\text{min}}^{\text{fmat}}$ and $\text{GDD}_{\text{max}}^{\text{fmax}}$ are the GDD for the beginning and end fruit filling, respectively. Each phytomer receives a fraction of the total fruit carbon pool given by:

$$A_{\text{fruit}}^p = \frac{S_p^{\text{fruit}}}{\sum_{p=1}^n S_p^{\text{fruit}}} \times A_{\text{fruit}} \quad \text{Eq. 9}$$

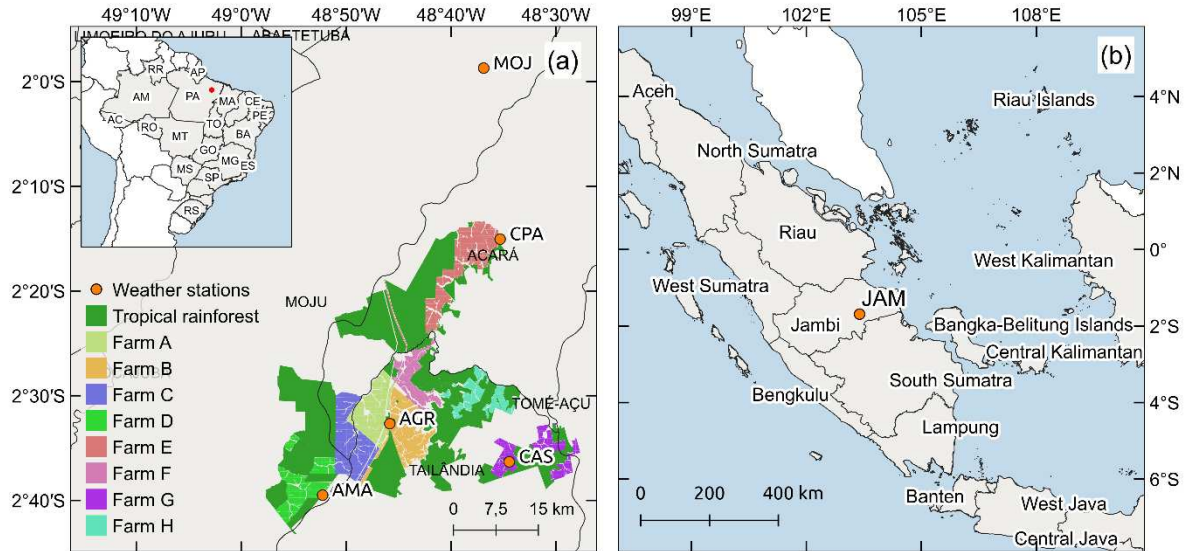
2.2. Region of study and experimental field data

2.2.1. Region of study

The study area is in the northeastern Pará state, in Brazil, in a commercial oil palm plantation (Figure 1a). There are eight farms covering 107,000 ha in four municipalities (Moju, Acará, Tailândia and Tomé-Açu), of which 39,000 ha are planted with oil palm and 64,000 ha are covered by tropical rainforest. Four weather stations, named Agropalma, Amapalma, CPA,

and Castanheira (hereinafter referred to as AGR, AMA, CPA, and CAS, respectively) are placed in four different farms.

Figure 1 – Maps of the region of study located in Brazil (a) and Indonesia (b).



Source: Author.

Oil palm has been cultivated in northeastern Pará since the second half of the 20th Century. Before the oil palm plantation, the Amazon Rainforest covered all region. From the petroleum crisis in the 1980s, the Brazilian government created programs to encourage the production of biofuels, such as the Pro-óleo (*Programa Nacional de Produção e Óleos Vegetais para Fins Energéticos*), which aimed to increase to 30% the amount of biodiesel in petroleum-derived diesel. (Feroldi, Cremonez and Estevam, 2014). Currently, the northeastern Pará is the major Brazilian producer.

The local climate is characterized by high rainfall amount ($\sim 2,800 \text{ mm yr}^{-1}$) and high air temperature and humidity throughout the year. The seasonality of rainfall is strong, with rainy summers (December to May) and drier winters (April to November). During the rainy season months, the precipitation is usually greater than 200 mm, reaching a peak in March ($\sim 500 \text{ mm}$). In the drier months, the precipitation reduces, but only in August and September, the rainfall amount is usually less than 100 mm. The average annual air temperature is 26°C and sometimes exceed 36°C in the warmer months. The relative humidity is high throughout the year, usually above 70%.

Besides the sites at commercial oil palm plantation, two micrometeorological towers provided data to calibrate and validate the model. The first (JAM, Figure 1b) is placed in a commercial oil palm plantation in the Jambi province, in Indonesia, near to Jambi City. The

annual precipitation is about 2,200 mm, with a rainy season during the first semester, peaking in December and March and a drier season during the second semester. The climate is hot, with a mean air temperature of 26°C (Stiegler *et al.*, 2019). The second site (MOJ, Figure 1a) is in a commercial plantation in the northeastern Pará, near to Moju City. The local climate is hot and humid, with an average air temperature of 26°C and relative humidity usually greater than 80%. The annual precipitation is about 3,000 mm, with strong seasonality. The rainy season starts in December and ends in June, raining more than 200 mm per month on average, peaking in March (Fonseca *et al.*, 2018). During the drier months, the precipitation reduces, but is usually greater than 100 mm.

2.2.2. Eddy covariance measurements

Two micrometeorological stations placed in JAM and MOJ sites (see section 2.1) provided data for model calibration and validation. Both micrometeorological stations are placed in commercial plantations and provide data of net radiation (R_n), sensible and latent heat fluxes (H and LE , respectively), ground heat flux (G), and net ecosystem CO_2 exchange (NEE). In the JAN site, eddy covariance instruments are placed in a 22 m high tower, while the G sensor is placed on 5 cm deep (Meijide *et al.*, 2017). In the MOJ site, eddy covariance instruments are placed in a 23 m high tower, and the G sensor is placed on 10 cm deep (Fonseca *et al.*, 2018). Eddy covariance measurements are available from March 2014 to December 2018 for JAM and from January 2015 to March 2016 for MOJ. In the JAM site, some data issues produce missing data from August 2016 to June 2017. In the MOJ site, a malfunction in the sonic anemometer produced poor-quality data after April 2016. The data sets were not subjected to any gap filling process.

Three post-processing methods were applied in both datasets to remove poor-quality data. First, the data flagged as class 2 according to the steady-state and integral turbulence characteristic test were removed (Mauder and Foken, 2006). Then, a filter was applied to the H and LE data in which the energy balance ($H + LE = R_n + G$) does not close by at least $\pm 40\%$. Last, it was applied the change-point detection method to find a friction velocity threshold ($u_{\text{threshold}}^*$) in which the atmospheric is stable due to the not well-developed turbulence condition (Barr *et al.*, 2013). All NEE value measured under $u^* \leq u_{\text{threshold}}^*$ was removed.

2.2.3. Climate data

The main source of climate data is the weather stations placed into the six sites. Table 1 presents the data period and climate variable available for each site. Data from JAM site is

available in a 30-minute interval, while the AGR, AMA, CPA, and CAS dataset sites are provided in a 15-minute interval, and the MOJ site dataset provides data every 10 minutes.

Table 1 – Climate dataset availability for the weather station placed in the studied sites

Site	Period of data available	Climate variables
JAN	Mar 2014 – Apr 2019	Air temperature, relative humidity, wind speed, precipitation, solar radiation, air pressure at the surface level
MOJ	Jan 2014 – Dec 2017	Air temperature, relative humidity, wind speed, precipitation, incoming and outgoing shortwave and longwave radiation, air pressure at the surface level
AGR	Jan 2012 – Dec 2018	Air temperature, relative humidity, wind speed, precipitation, solar radiation
AMA	Jan 2013 – Dec 2018	Air temperature, relative humidity, wind speed, precipitation, solar radiation
CPA	Dec 2012 – Dec 2018	Air temperature, relative humidity, wind speed, precipitation, solar radiation
CAS	Jan 2013 – Dec 2018	Air temperature, relative humidity, wind speed, precipitation, solar radiation

Source: Author.

The weather station datasets presented a large number of low-quality and missing data values. It was considered low-quality all impossible or very unlikely values (for example, negative relative humidity and air temperature above 60°C, respectively). All low-quality data was removed from the dataset, producing even more missing data in the time series. Also, model experiments require a complete time series. So, the weather station datasets were integrated to an hour and filled all missing values using the ERA5 dataset (C3S, 2017). Air pressure at the land surface was provided by ERA5 for AGR, AMA, CPA, and CAS sites.

Additionally, two daily gridded climate datasets were used to provide older data for the weather stations as required. The first dataset is the Brazil Gridded Meteorological Data (hereinafter referred to XAV), which is an interpolation product of several Brazilian rain gauges and weather stations (Xavier, King and Scanlon, 2016). The second dataset (hereinafter referred to NPW) is a reanalysis provided by NASA POWER Project (Sparks, 2018).

2.2.4. Yield database

We use yield data from a data set provided by the commercial plantation previously referred, placed in northeastern Pará, Brazil, to compare with the yield simulated by the model. The plantation is divided into eight farms (named from A to H) and each farm into several plots (see Fig. 1a). The production database provides yield data from 2004 (or after for younger plots) to 2018 for all plots of all farms, except for farm F, which was not addressed in this study. There are plots planted in different years on the same farm, so all plots placed on the same farm and planted in the same year were grouped by averaging, producing 56 groups. The plot groups were also grouped according to the variety planted into its plots. Table 2 presents the list of varieties and the proportion of each one per farm.

Table 2 – List of varieties per farm. The superscripts represent the proportion of the variety in the farm, where *** $\geq 50\%$, ** $\geq 25\%$, * $\geq 10\%$, and fs (few samples) $\geq 5\%$. Less than 5% is not shown. The variety names are according to the provided database

Farm	Variety (proportion)
A	Deli X La Mé ^{***} , Deli X Yangambi [*] , Deli X Avros [*] , Deli X Ghana ^{fs}
B	Deli X La Mé ^{**} , Deli X Avros ^{**} , Deli X Ghana [*] , Deli X Ekona ^{fs} , Deli X Yangambi ^{fs}
C	Deli X La Mé [*] , Deli X Ghana [*] , Deli X Ekona [*] , Deli X Avros [*] , Deli X Kigoma ^{fs} , Dami ^{fs}
D	Deli X La Mé [*] , Deli X Gana [*] , Deli X Ekona [*] , Deli X Avros [*] , Deli X Kigoma [*] , Deli X Congo [*]
E	Deli X La Mé ^{**} , Deli X Ghana [*] , Deli X Ekona [*] , Deli X La Mé / Yangambi [*]
G	Deli X La Mé ^{**} , Deli X Ghana ^{fs} , Deli X Avros [*] , Deli X Nigeria [*] , Compacta X Gana [*] , Compacta X Nigeria [*] , Deli X Nigeria / Compacta Ghana ^{fs} , Deli X Avros / Deli X Compacta ^{fs}
H	Deli X La Mé [*] , Deli X Ghana [*] , Deli X Ekona ^{fs} , Deli X Nigeria ^{fs} , Compacta X Ghana ^{fs} , Compacta X Nigeria ^{fs} , Deli X Compacta ^{fs} , Tanzania X Ekona [*] , Compacta X Ekona ^{fs}

Source: Author.

2.2.5. Soil properties

The database available for this study did not provide field measurements of soil properties in any of the sites studied. Due to this lack of information, the global database

SoilGrids250m were used (Hengl *et al.*, 2017). The database uses field measurements from 150,000 soil profiles worldwide to train the machine learning model and uses remote sensing data to provide information about soil properties across the globe in a 250 m horizontal resolution and seven soil layers (0 cm, 5 cm, 15 cm, 30 cm, 60 cm, 100 cm, and 200 cm deep). In this study, information about clay, silt, and sand content and the soil bulk density were provided by the SoilGrids250m database from 5 cm to 200 cm. Also, other soil properties required by the model, such as field capacity and permanent wilt point, saturated hydraulic conductivity and porosity were estimated through empirical equations that consider the soil properties provided by SoilGrids250m database (Clapp and Hornberger, 1978; Cosby *et al.*, 1984).

2.3. Model calibration and validation strategies

2.3.1. Sensitivity analysis and calibration

A model sensitivity analysis determines how the variation of a parameter value affect the model performance to simulate a variable. The sensitivity analysis aids to reduce the number of parameters that need to be calibrated.

The sensitivity analysis and the parameters calibration were performed using the JAM site data. First, 2,000 simulations were performed using a set of parameter values randomly chosen within a predefined range and used by oil palm PFT for each simulation. The input climate data was provided by NPW dataset from 2002 (planting year) to 2013 and from the JAM weather station from 2014 to 2018. Then, the model performance was evaluated to simulate H, LE, and NEE by MAE (mean absolute error) as followed:

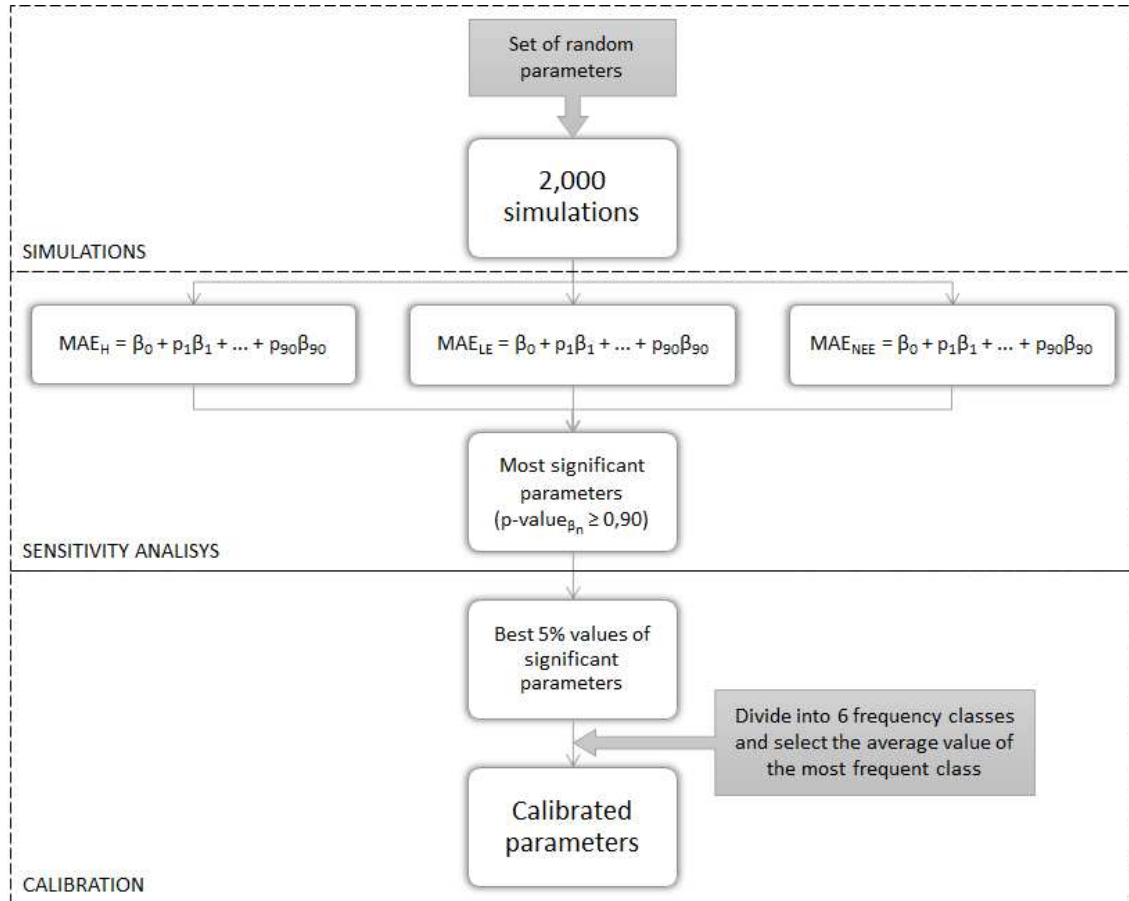
$$MAE = \frac{1}{n} \sum_{i=1}^n |P_i - O_i| \quad \text{Eq. 10}$$

where n is number of available data and P_i and O_i is i-th predict and observed values of a variable, respectively.

The model sensitivity was evaluated by fitting three multiple linear regressing among the MAE of H, LE, and NEE and all parameter values used in the simulations. It was considered that the model was sensitive to parameters in which the corresponding coefficient (β_i) was significant at 90% probability. For the model calibration, were selected the parameters that performed the 5% best simulations for the three evaluated variables and aggregated into six

frequency classes. The average value of the most frequent class was selected as the calibrated parameter. Figure 2 shows the diagram that summarizes the sensitivity analysis and the calibration framework.

Figure 2 – Diagram of the sensitivity analysis and model calibration.



Source: Author.

2.3.2. Model validation

Model performance was validated to simulate the components of energy (R_n , H , and LE) and carbon (NEE) balance on the land surface and compared to the observed field measurements from the MOJ site. The simulation was carried out from 2006 (planting year) to 2017 using the set of calibrated parameters. The model climatic input was the XAV dataset from 2006 to 2014 and MOJ weather station data from 2014 to 2017. Due to the limited eddy covariance time series length, the validation period was from January 2015 to April 2016.

Some statistics were used to estimate the error of the simulation concerning eddy covariance measurements. A regression analysis was performed to estimate the goodness to fit between hourly simulated and observed data through the R^2 (coefficient of determination). Also, the MAE and RB (relative bias, Eq. 11) were used to estimate the model accuracy.

$$RB = 100 \times \frac{\sum_{i=1}^n |P_i - O_i|}{\sum_{i=1}^n |O_i|} \quad \text{Eq. 11}$$

where n is number of available data and P_i and O_i is i -th predict and observed values of a variable, respectively. The RB is able to show that the model is underestimating (negative values) or overestimating (positive values) the observed data, so that the closer to zero, the better the model's performance.

2.4. Oil palm carbon uptake and assimilation

The effects of climatic factors, such as air temperature and vapor pressure deficit (VPD) on carbon uptake and assimilation by the oil palm were evaluated, as well as the model's performance to simulate this relationship. The water and light use efficiency (WUE and LUE, respectively) were calculated according to the following equations to assess the relationship between carbon uptake and assimilation by the oil palm and the climate factors:

$$WUE = \frac{NEP}{ET} \quad \text{Eq. 12}$$

$$LUE = \frac{NEP}{PAR_{in} - PAR_{out}} \quad \text{Eq. 13}$$

where NEP is the monthly mean of net ecosystem productivity ($\text{g-C m}^{-2} \text{ s}^{-1}$), ET is evapotranspiration (mm s^{-1}), and PAR_{in} and PAR_{out} are the incident and reflected photosynthetically active radiation, respectively ($\text{MJ m}^{-2} \text{ s}^{-1}$). NEP is measured directly using the eddy covariance technique ($NEP = -NEE$). Both WUE and LUE were estimated only for the daytime period (between 6:00 and 18:00).

The WUE and LUE analysis were divided according to the air temperature and the VPD into two parts. First, it was assessed how WUE and LUE vary according to air temperature and VPD on an hourly scale to understand the impact of these climatic factors on the carbon assimilation of oil palm plantations. It was also assessed the ability of the model to reproduce the behavior of WUE and LUE with air temperature and VDP. In the second part, it was calculated the mean of each month for both WUE and LUE to assess the behavior throughout the year. The ability of the model to simulate the monthly variation of both WUE and LUE was assessed. In both analyzes, the evaluation was performed only in 2015, since only the first three months of 2016 have data available.

2.5. Yield simulations

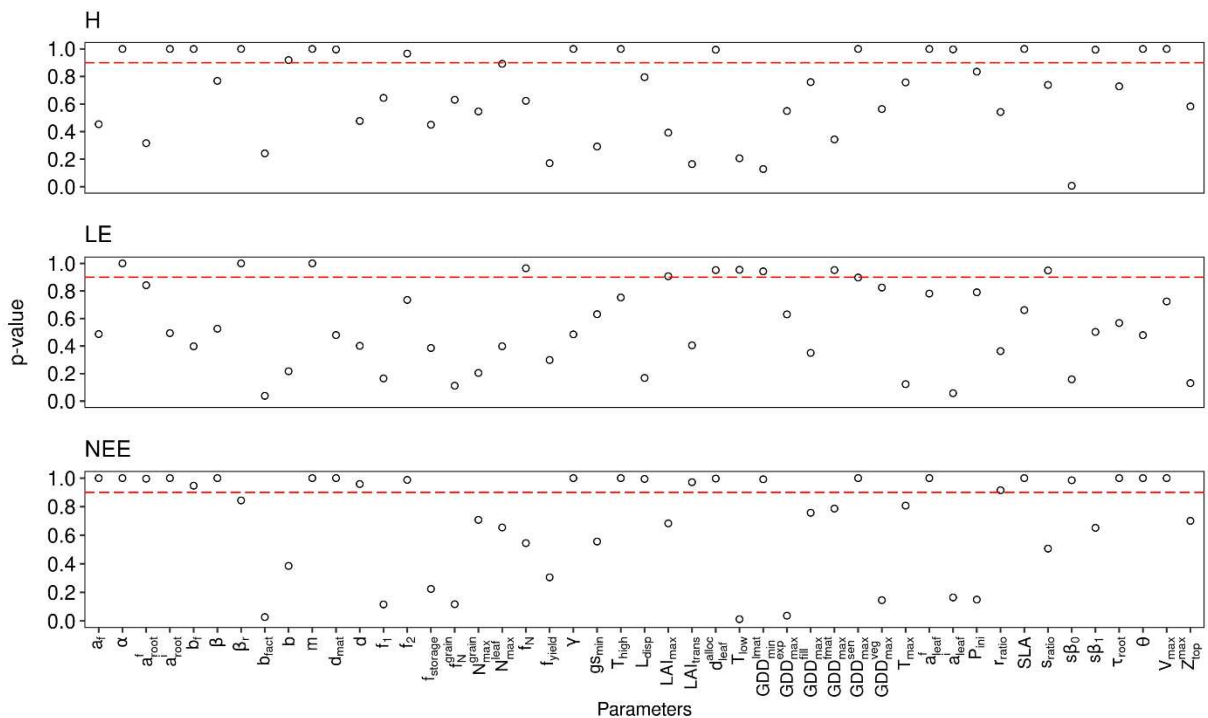
Oil palm yield is strongly dependent on endogenous factors, such as plant age, as well as external factors, such as soil, crop management, and climate. To consider these factors, the oil palm yield was evaluated in relation to planting age and per farm. The simulations of the yield of each group of plots were ran using the climatic data from the weather station closest to the centroid of the group of simulated plots. To simulate the yield of the groups of plots planted before the beginning of the period of available data from the nearest weather station, the XAV data set was also used. The set of parameters used in all simulations corresponds to that calibrated according to section 2.3.1. The average monthly yield was also assessed for the farms as a whole and for each farm individually, as well as the performance of the model to simulate the crop yield for each month. The variation in yield among plots of each farm was also assessed using the coefficient of variation (CV) as the statistical metric. The CV is the ratio between the standard deviation and the average, so that the higher the CV, the greater the dispersion of yield on the evaluated farm.

3. RESULTS

3.1. Sensitivity analysis and calibration

The proposed sensitivity analysis framework was able to identify the most sensitive parameters to simulate energy and carbon fluxes. Figure 3 presents the 33 parameters that significantly affect the simulation of at least one variable (H, LE, and NEE) on JAM site. NEE simulation was sensitive to the largest number of parameters, followed by H and LE (24, 18, and 10 parameters, respectively). For four parameters, the model was shown to be sensitive to simulate all variables simultaneously (H, LE, and NEE), whereas for 13 parameters the model was sensitive to the simulation of two of them. Finally, the model was shown to be sensitive to 17 parameters to simulate only one variable.

Figure 3 – List of parameters that the model showed to be sensitive to simulate H, LE, and NEE. Black circles represent the p-value of the parameter coefficients of the linear regression fitted between the MAE of the simulations and the values of the parameters. The dashed red line represents the 90% probability threshold for considering that the model was sensitive to the parameter to simulate H, LE, and NEE. Parameters description could be found in Table 3



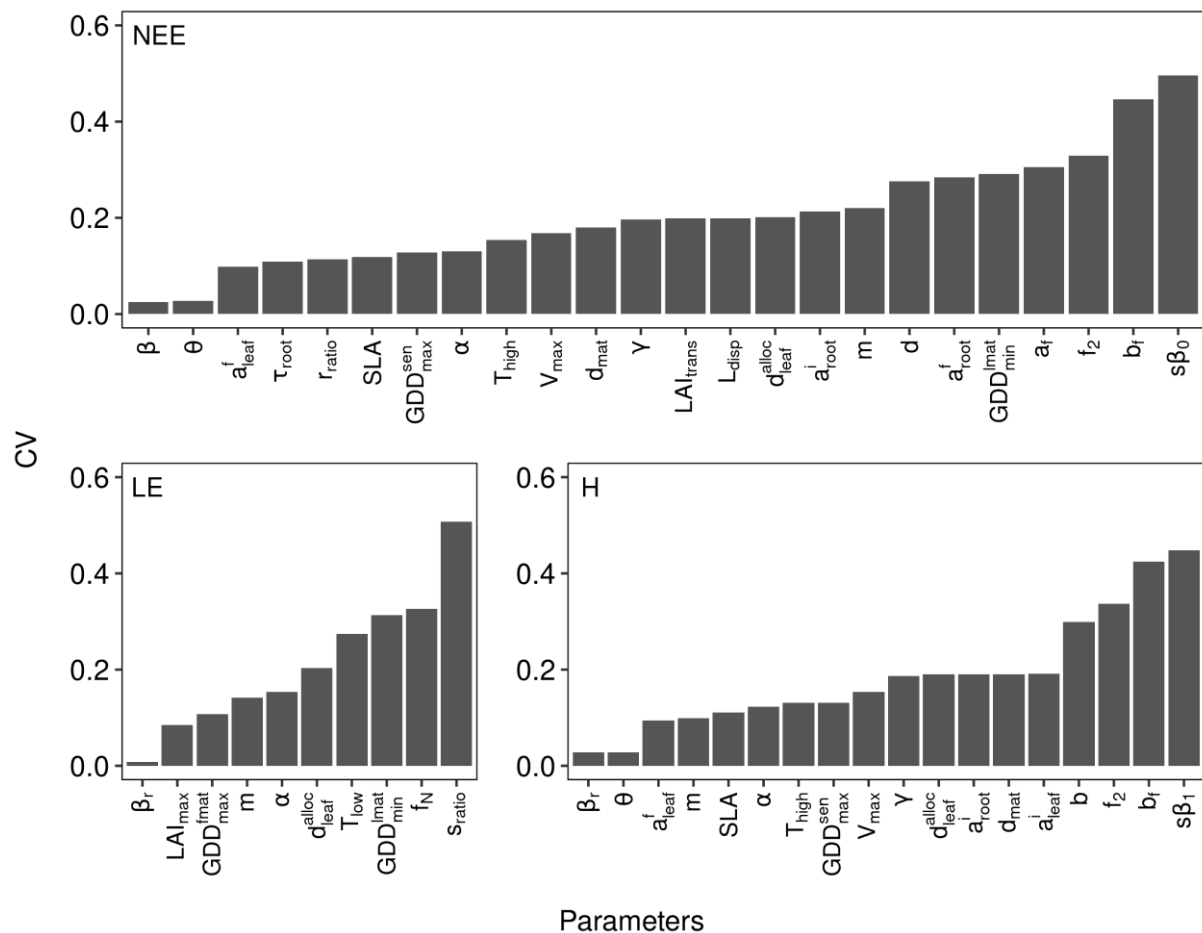
Source: Author.

As expected, NEE simulation was shown to be sensitive mainly to photosynthesis, plant respiration, and leaf carbon allocation parameters. The parameters that control the allocation of carbon and specific leaf area (SLA) affect the LAI, which provides an interface between solar radiation and photosynthetic cells, whereas parameters that control

photosynthesis and leaf respiration affect the rate of net carbon assimilation. LE was mainly sensitive to stomatal conductance, cumulative root fraction, and leaf growing control parameters since this flux is related to the water change phase by evaporation in the ecosystems. So, the root distribution in the soil profile controls the amount of soil water available to the plant, and stomatal conductance couple to photosynthesis controls the leaf stomata aperture. Consequently, these processes regulate the water loss by leaves, affecting the LE. Last, the H simulation depends on the air temperature profile (Sellers, 1997). Most of the energy used to heat the air is provided by the soil, which was previously heated by the absorbed solar radiation which passed through the canopy. In addition, the heat transfer within the soil and between the soil and the overlying atmosphere is regulated by the soil thermal conductivity, which is affected by its physical properties (e.g. particle size, mineralogy) and the degree of saturation (Zhang and Wang, 2017). Thus, the model is more sensitive in the simulation of H to the parameters that control the LAI, which controls the amount of radiation that reaches the ground, as well as those related to water loss by evapotranspiration, which controls the soil water content.

The model parameter uncertainty was analyzed using the CV of the parameters that performed the 5% best simulation results of H, LE, and NEE (Figure 4). The results showed that the uncertainty of β and θ parameters was low for NEE, whereas the β_r and θ parameters presented the lower uncertainty for H, and β_r was the parameter with the lower uncertainty in the LE simulation. Also, the uncertainty of the parameters common to two or more calibrated variable was almost always similar. The parameter m , for example is an exception to this rule since the CV of the parameter for H is almost half of the CV for NEE. Besides to showing the uncertainty of the parameters in the simulation of H, LE, and NEE, Figure 4 also gives an idea of how sensitive the model is for each parameter. A low CV implies that the best results of the simulations were achieved in a small range of parameter values, meaning that small variations in the parameter value considerably reduce the performance of the model. Thus, the smaller the CV, the more sensitive the model is to the parameter. Indeed, the simulation of H and LE, for example, shown to be sensitive to the β_r parameter, since the β_r parameter controls the distribution of fine roots in the soil profile. Thus, both evapotranspiration, which affects the LE simulation, and the thermal conductivity of the soil, which affects the H simulation, are strongly dependent on the β_r value.

Figure 4 – Coefficient of variation (CV) of the parameters that performed the 5% best simulation results for H, LE, and NEE.



Source: Author.

In the calibration process, the parameter value calibrated for each variable individually was estimated, according to the proposed methodology. The final calibrated value for each parameter was obtained by averaging the calibrated values for each variable individually. Some parameters showed quite different values for the calibration of H, LE, and NEE. For example, the value of parameter α was 45.9% lower for NEE than the calibrated value. For H and LE, the difference was only 18.4% and 8.3%, respectively. Table 3 presents the parameters that the model was most sensitive to and calibrated values.

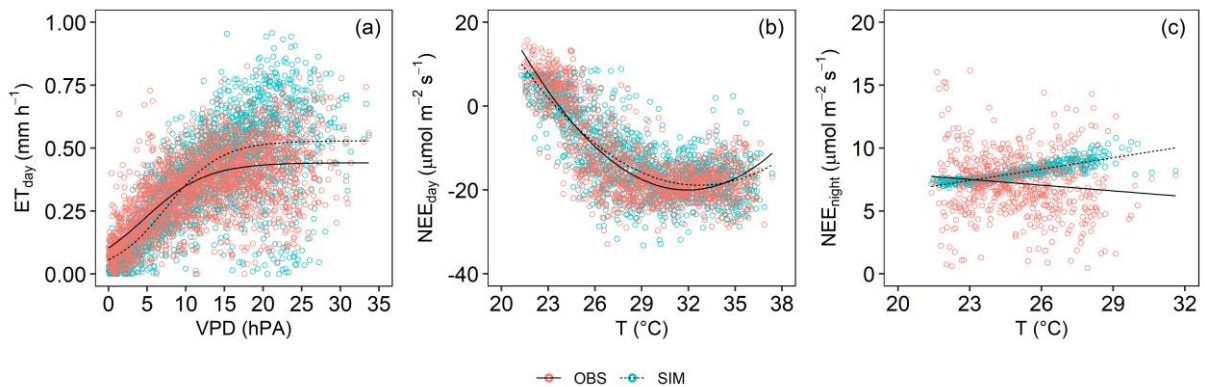
Table 3 – Summary of parameter values calibrated to simulate H, LE, and NEE

Parameter	Description	Sensitive to simulate	Calibrated value	Unit
α	Intrinsic quantum efficiency	H, LE, and NEE	0.074	-
β	Photosynthesis coupling coefficient	H and NEE	0.94	-
θ	Photosynthesis coupling coefficient	H and NEE	0.94	-
γ	Leaf respiration coefficient	H and NEE	0.017	mol mol ⁻¹
m	Coefficient m of stomatal conductance equation	H, LE, and NEE	10.4	mol m ⁻² s ⁻¹
d	Drought index	NEE	1.02	-
b	Coefficient b of stomatal conductance equation	H and NEE	0.004	mol m ⁻² s ⁻¹
V_{\max}	Maximum rate of Rubisco carboxylase enzyme activity	H, LE, and NEE	9.1 x 10 ⁻⁵	mol m ⁻² s ⁻¹
SLA	Specific leaf area	H and NEE	13	m ² kg-C ⁻¹
τ_{root}	Fine root biomass turnover time constant	H and NEE	1108	years
β_r	Cumulative fine root fraction	H, LE, and NEE	0.98	-
$s\beta_0$	Water stress factor	NEE	-34.5	-
$S\beta_1$	Water stress factor	H	555	-
T_{high}	High-temperature threshold in the V_{\max} temperature-dependence equation	H and NEE	40.3	°C
T_{low}	Low-temperature threshold in the V_{\max} temperature-dependence equation	LE	8.2	°C
f_2	Parameter in the V_{\max} temperature-dependence equation	H	0.36	-
a_{root}^i	Initial root allocation coefficient	H and NEE	0.28	-
a_{root}^f	Final root allocation coefficient	NEE	0.10	-
r_{ratio}	Leaf:root N allocation ratio	NEE	0.73	-
s_{ratio}	Leaf:stem N allocation ratio	NEE	0.02	-
f_N	Minimum leaf nitrogen content that does not experience N stress	LE	0.03	g-N
a_{leaf}^i	Initial leaf allocation coefficient	H	0.18	-
a_{leaf}^f	Final leaf allocation coefficient	H and NEE	0.28	-
d_{mat}	Age-controlling parameter in the leaf allocation equation	H and NEE	0.61	-
$d_{\text{leaf}}^{\text{alloc}}$	Shape-controlling parameter of the leaf allocation equation	H and NEE	0.54	-
a_f	Controlling the base value of the fruit bunches C allocation equation	NEE	0.12	-
b_f	Controlling the shape of the curve in the fruit bunches C allocation equation	H and NEE	0.04	m ² g-C ⁻¹
L_{disp}	Unopen/open leaf C allocation ratio	H and NEE	0.24	-
LAI_{trans}	Leaf area index in the transplanting	NEE	0.18	m ² m ⁻²
LAI_{max}	Maximum allowable LAI	LE	6.4	m ² m ⁻²
$GDD_{\text{max}}^{\text{sen}}$	Thermal time from leaf expansion to end of senescence for each phytomer	H and NEE	8217	°C
$GDD_{\text{max}}^{\text{fmat}}$	Thermal time from the beginning to end of fruit filling for each bunch	H and NEE	6033	°C
$GDD_{\text{min}}^{\text{lmat}}$	Thermal time from leaf opening to leaf maturity for each phytomer	NEE	1118	°C

Source: Author.

The calibration was efficient for the adjustment of the parameters related to the evapotranspiration process. The behavior of the simulated evaporation in relation to the VPD was similar to the measured, showing that the parameters that control the stomatal conductance and the water uptake by roots was close to the expected (Figure 5a). In addition, the calibration was able to adjust good parameters to simulate the response of carbon assimilation during the day (NEE) to air temperature. This relationship must be well represented by the model since the photosynthetic rate responds to the air temperature (Sage and Kubien, 2007). However, the response of the NEE to the air temperature during the night, when the carbon flux comes from ecosystem respiration, did not correspond to that measured in the field (Figure 5c). The results show that the NEE grows linearly with the air temperature, but the field measurements showed that the ecosystem respiration varied widely for the same air temperature range. Indeed, ecosystem respiration does not only depend on air temperature, but on other factors such as soil moisture, which could cause non-linearity in the relationship between NEE and air temperature (Chen *et al.*, 2019; Wen *et al.*, 2006). In addition, there is great uncertainty in NEE measurements by the eddy covariance method at night, when the atmospheric boundary layer stability conditions, in general, are not ideal.

Figure 5 – Behavior of (a) evapotranspiration (ET) in relation to the variation of the vapor pressure deficit (VPD) and the net ecosystem productivity (NEE) variation during the day (b) and at night (c) in relation to the air temperature. The red and blue circles correspond to the measured and simulated data, respectively



Source: Author.

3.2. Energy and carbon fluxes simulation

3.2.1. Model validation

The model performance to simulate the hourly energy and carbon fluxes for MOJ site varied widely according to the assessed variable. It is noteworthy that both energy and carbon

fluxes data were previously filtered, as presented above (section 2.2.2). In addition, the simulated data corresponding to the observed missing values were also removed. Table 4 shows the amount (in hours) and the percentage of data remaining after filtering.

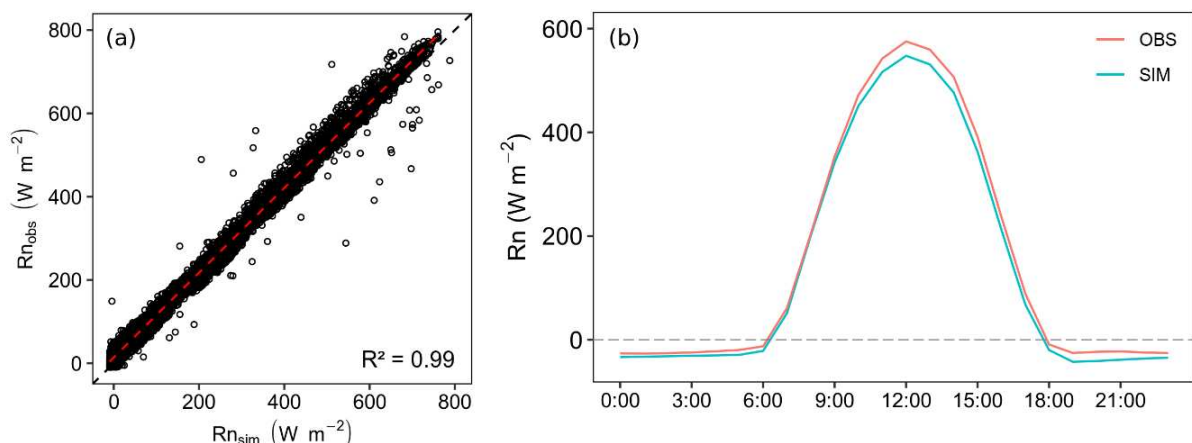
Table 4 - Amount (and percentage) of data before and after filtering

Variable	Data amount before filtering	Data amount after filtering
Rn	62,410 (89%)	62,410 (89%)
H	17,924 (51%)	2,633 (8%)
LE	1,6049 (46%)	2,633 (8%)
NEE	1,6855 (48%)	7,059 (20%)

Source: Author.

Rn long-term mean simulated slightly underestimated the measurements, with a relative bias of -9.86%. The low MAE of 19.04 W m^{-2} compared to the variable diurnal magnitude and a very high R^2 (Figure 6a) for the linear regression fitted between simulated and observed data showed that the model was accurate to simulate Rn. In addition, the simulated Rn followed similar diurnal cycle behavior compared to the measurements, underestimating a bit from 9:00 to 15:00 (Figure 6b).

Figure 6 – Linear regression fitted between observed and simulated net radiation (a), and the simulated (blue line) and observed (red line) net radiation diurnal cycle (b) for MOJ site. R^2 is the coefficient of determination

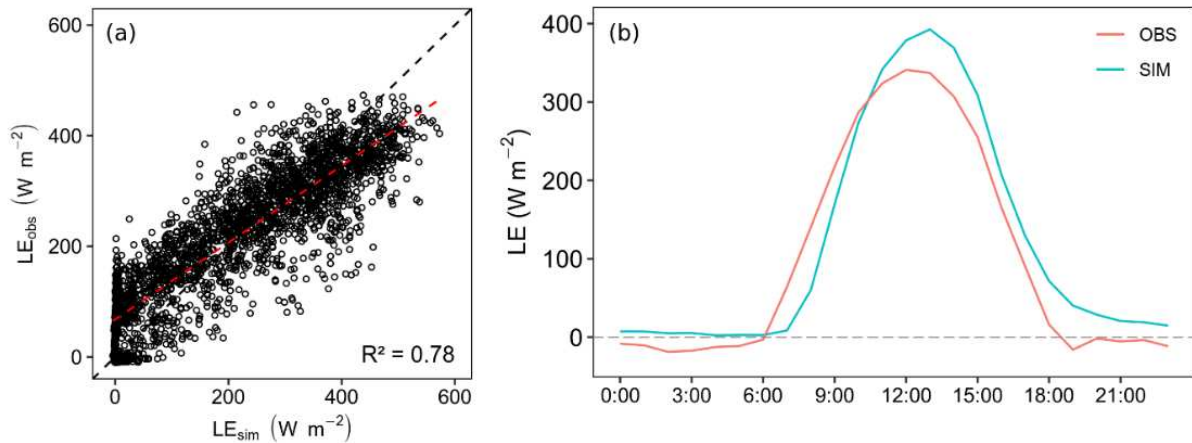


Source: Author.

The simulated LE also achieved a good agreement with the measurement data, with a low relative bias of 0.96% and a high R^2 (Figure 7a). However, the high MAE of 59.16 W m^{-2} compared to the variable diurnal amplitude showed that the bias is widely spread around zero (CV of the bias was 1,785%). Diurnal cycle behavior of simulated LE was similar to the

observed data but delayed by one hour. This delay causes an underestimation of the lowest LE values ($< 250 \text{ W m}^{-2}$) and an overestimation of the highest values, raising the MAE. Therefore, the simulated daytime peak of LE around noon is higher than the observed data (Figure 7b).

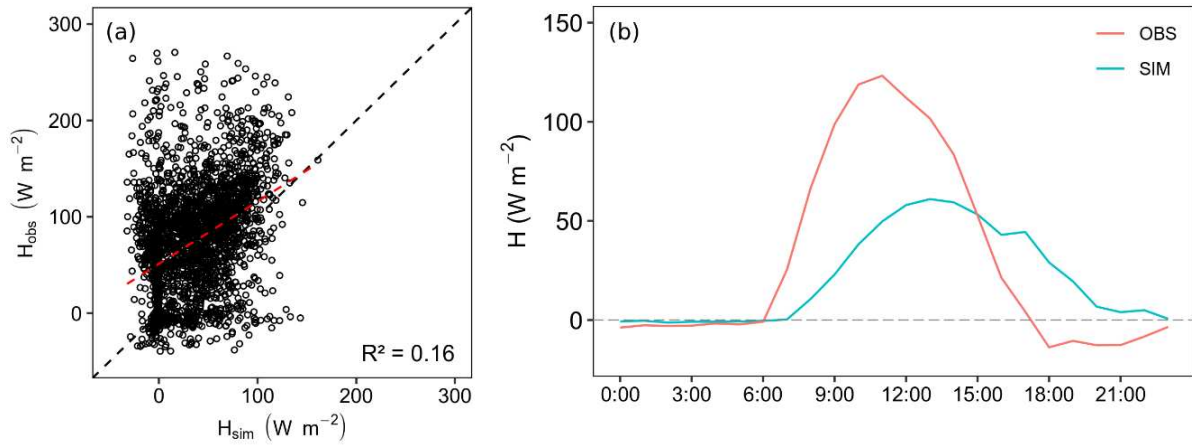
Figure 7 – Linear regression fitted between observed and simulated latent heat flux (a), and the simulated (blue line) and observed (red line) latent heat flux diurnal cycle (b) for MOJ site. R^2 is the coefficient of determination



Source: Author.

Poor agreement was achieved between simulated and observed sensible heat flux, with a relative bias of -54.16%. The Long-term simulated and observed mean were quite different, and the low R^2 (Figure 8a) and the high MAE of 51.16 W m^{-2} compared to the flux diurnal amplitude showed that the model was not able to simulate H accurately. The diurnal cycle of H was flattened and delayed compared with field measurements. The model did also not well simulate the amplitude of the diurnal cycle (Figure 8b).

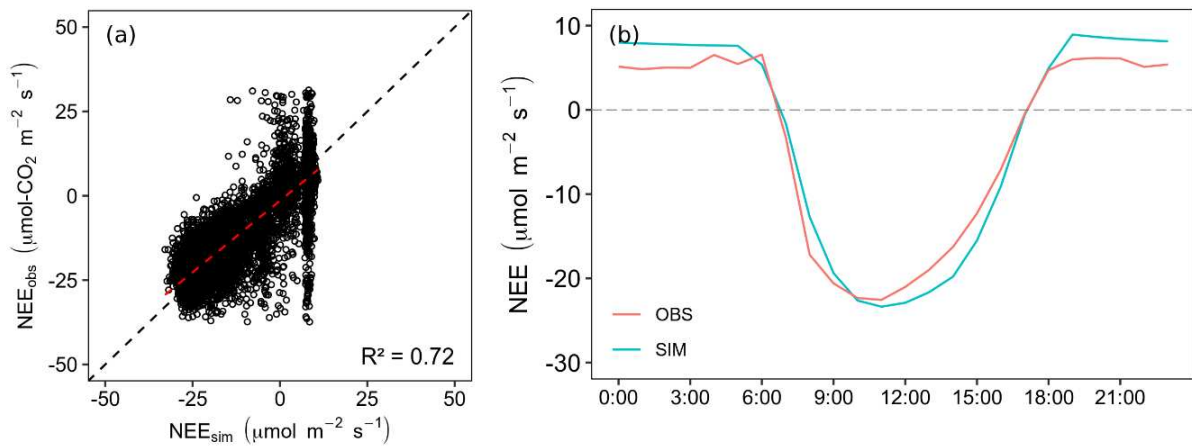
Figure 8 – Linear regression fitted between observed and simulated sensible heat flux (a), and the simulated (blue line) and observed (red line) sensible heat flux diurnal cycle (b) for MOJ site. R^2 is the coefficient of determination



Source: Author.

Last, NEE was simulated with an satisfactory agreement, with relative bias of -16.01% and a high R^2 (Figure 9a). Diurnal cycle behavior was well simulated, as well as the diurnal amplitude. The CO_2 source-to-sink transition at 7:00 of the simulated NEE agreed with the observation, as well as the transition of sink-to-source at 17:00 (Figure 9b).

Figure 9 – Linear regression fitted between observed and simulated net CO_2 ecosystem exchange (a), and the simulated (blue line) and observed (red line) net CO_2 ecosystem exchange diurnal cycle (b) for MOJ site. R^2 is the coefficient of determination



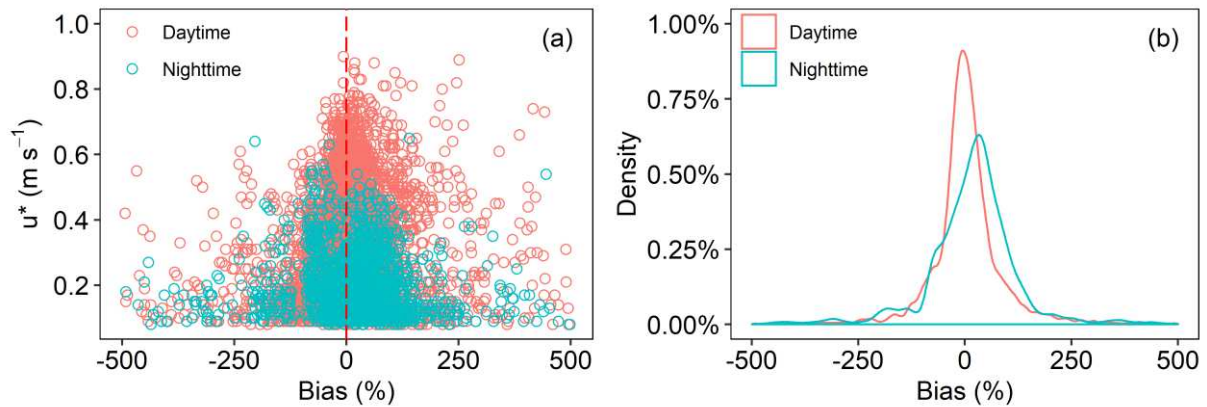
Source: Author.

The set of parameters calibrated from the data provided by the JAM site proved to be well adjusted to simulate the R_n , the NEE and the LE of the MOJ site, while the H simulation was poor. The small overestimation of R_n around noon is mainly related to the lack of information about the optical properties of the plant and the leaves orientation. In turn, the problems found in the LE and H simulation seem to have a similar origin. As explained earlier,

the sensible heat flux depends on the heat exchange between the land surface and the atmosphere. The lack of good quality information about the soil physical-hydric properties affects the simulation of thermal conductivity. This issue affects the H simulation more than the LE simulation, since most of the latent heat flux originates in plant transpiration, while the air temperature gradient is directly affected by the energy exchange at the soil-atmosphere interface.

Additionally, despite the good overall performance in the NEE simulation, the MAE of $5.71 \mu\text{mol m}^{-2} \text{s}^{-1}$ was relatively high when compared to the daytime amplitude. This controversial result was probably due to the poor result in the NEE simulation under low turbulence conditions (low u^*), mainly during the night, when there is a high uncertainty in the estimated NEE from the sensors. Figure 10a shows that the bias is low (close to zero) under high turbulence conditions and high otherwise. In addition, NEE tends to be overestimated during the night (median bias of 25%), so that more than 60% of the nighttime carbon flux bias is greater than zero. On the other hand, the bias is well distributed around zero during the daytime, with median of 1.2% (Figure 10b).

Figure 10 – Distribution of the NEE bias (%) according to the friction velocity (u^* ; m s^{-1}) and according to the frequency (a and b, respectively) for MOJ site. Light red present the daytime NEE bias and the light blue is the nighttime NEE bias in both frames



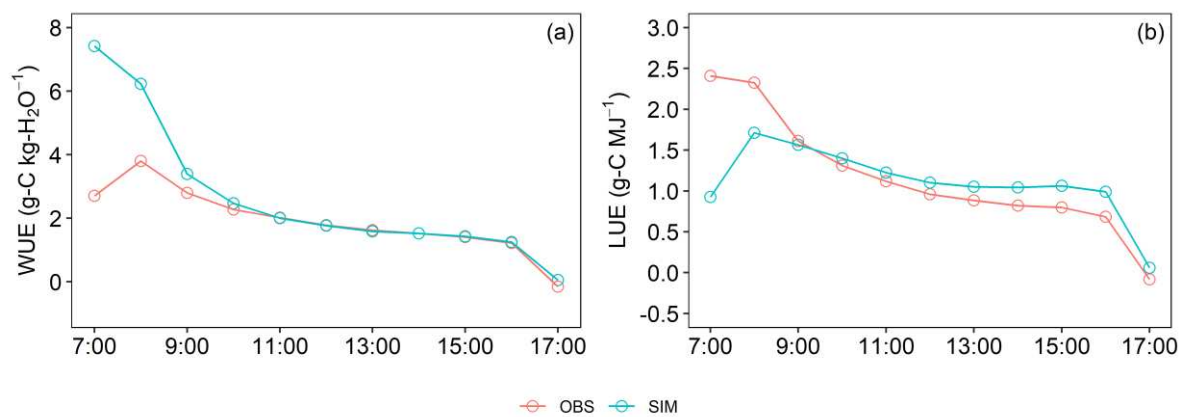
Source: Author.

3.2.1.1. Oil palm carbon uptake and assimilation

Daytime (from 07:00 to 17:00) water and light use efficiency for oil palm were evaluated on hourly and monthly time scales. On hourly timescale, both WUE and LUE were higher in the morning, just after sunrise (Figure 11Figure 12). Throughout the day both WUE and LUE steadily decrease, but at a lower rate from 11:00 to 16:00. At 17:00, both WUE and

LUE drop sharply to an efficiency close to zero. The model was able to simulate with good accuracy WUE and LUE on an hourly time scale after 09:00, but overestimated WUE and underestimated LUE from 07:00 to 08:00. However, it is observed that during the first hours of the day, atmospheric stability conditions are not favorable for the eddy covariance technique measurements. Therefore, part of the lack of fit between the simulated and observed data close to the sunrise may be due to measurement issues.

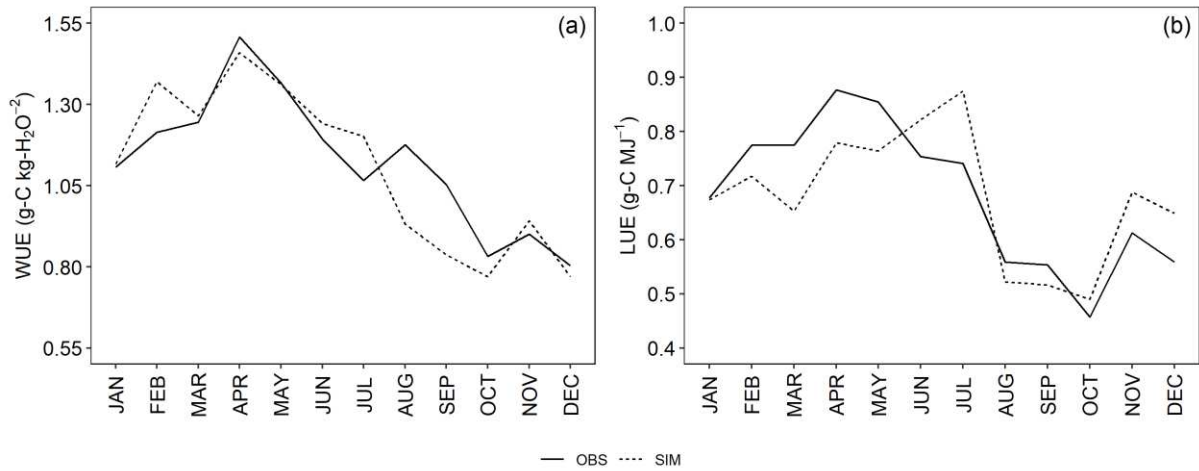
Figure 11 – Daytime average of WUE (a) and LUE (b) for the MOJ site. The circles and lines in red represent the measured values, while the circles and lines in blue show the results of the simulation



Source: Author.

On a monthly timescale, oil palm was more efficient (above the monthly average) in the water and light use in the first half of the year (Figure 12). From March to May, the oil palm reached maximum monthly efficiency, peaking in April, with WUE of 1.5 g-C kg-H₂O⁻¹ and LUE of 0.88 g-C MJ⁻¹. During the second half of the year, the efficiency in the use of water and light was reduced, mainly in the last three months. The WUE reaches its lowest value in December (0.8 g-C kg-H₂O⁻¹), while the LUE reaches the minimum in October (0.46 g-C MJ⁻¹).

Figure 12 – Monthly daytime of (a) water use efficiency (WUE) and (b) light use efficiency (LUE) in 2015 for MOJ site. Solid and dashed lines show the observed and simulated values from both WUE and LUE, respectively

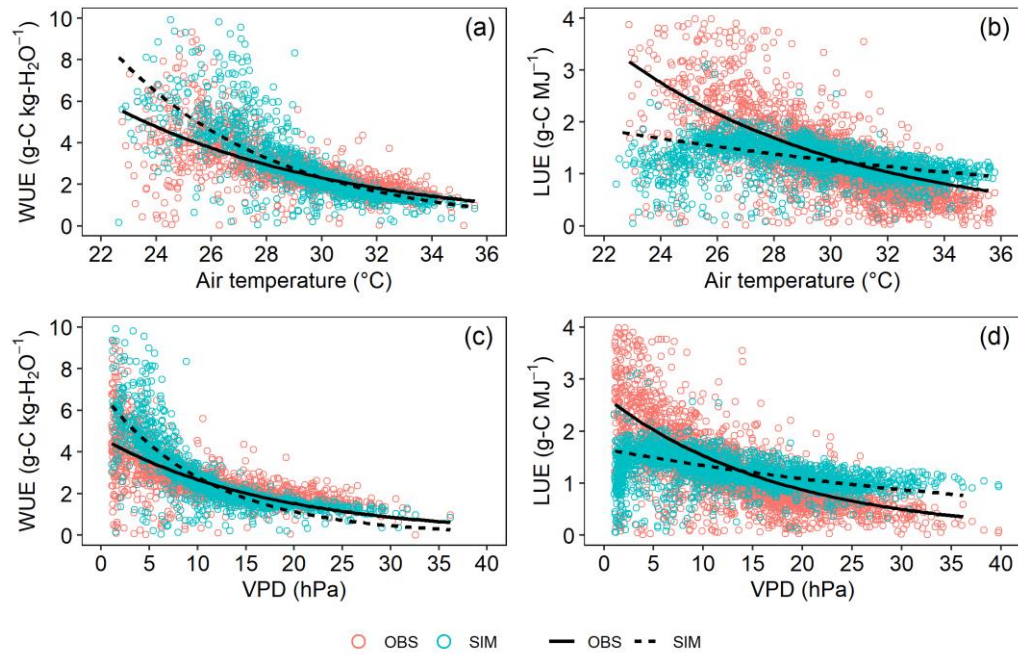


Source: Author.

The model also simulated WUE and LUE well on a monthly timescale, so that there was no statistically significant difference between the simulated and measured data (t-test $\alpha = 0.05$). The monthly mean of the measured WUE was 1.1 ± 0.2 g-C kg-H₂O⁻¹, while the model reached an average of 1.0 ± 0.3 g-C kg-H₂O⁻¹ (t-test p-value = 0.41). In the same period, the measured monthly LUE was 0.14 ± 0.03 g-C MJ⁻¹, while the model estimated it at 0.13 ± 0.03 g-C MJ⁻¹ (t-test p-value = 0.33). The monthly behavior of WUE and LUE was also well simulated by the model, so that the simulated high efficiency period was also the first half of the year, with WUE peaking in April (1.5 g-C kg-H₂O⁻¹), but with LUE peaking in July (0.87 g-C MJ⁻¹). In addition, the period of minimum efficiency in the water and light use was also well simulated, so that both WUE and LUE reached the lowest value in October (0.8 g-C kg-H₂O⁻¹ and 0.49 g-C MJ⁻¹, respectively).

In addition to the monthly variation of WUE and LUE, the efficiency in the water and light use according to the air temperature and the VPD was evaluated. Both WUE and LUE observed were sensitive to air temperature and VPD variation, so that the efficiency of carbon assimilation reduces to an exponential decay rate when air temperature and VPD rise (Figure 13). However, the variation in air temperature and VPD affects WUE more strongly than LUE. Note that WUE decreases by up to 90% with an increase of 14°C or 35 hPa, whereas LUE decreases by only 12% for the same range of air temperature and VPD. Simulated WUE presented the same behavior of the observed data, but a bit more sensitive than the observed for both air temperature and VPD. In turn, LUE was simulated with low sensitivity for both air temperature and VPD, compared to the observed.

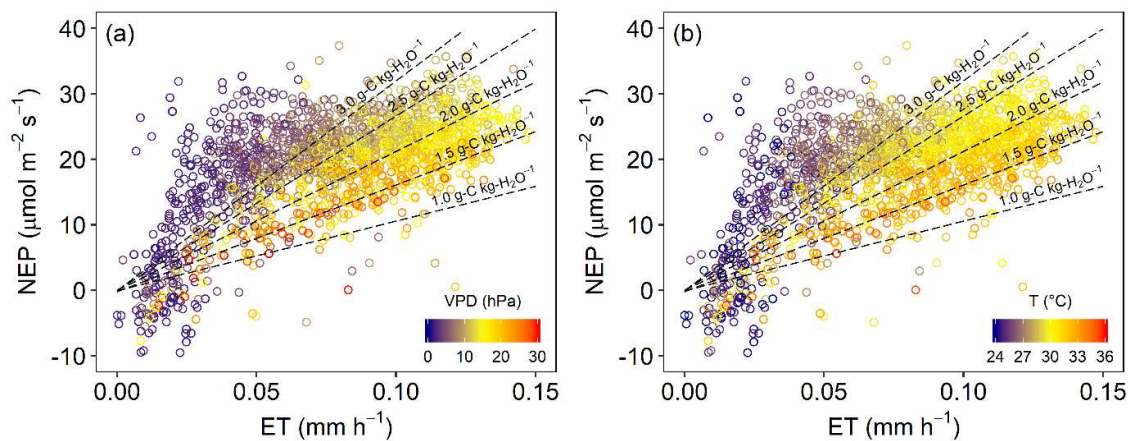
Figure 13 – Water and light use efficiencies variation in relation with air temperature (a and c) and vapor pressure deficit (b and d). Solid and dashed line presented the exponential decay curve for observed and simulated data, respectively



Source: Author.

It was also analyzed in this study how and what factors limit the efficiency in the use of water and light. Figure 14 shows that air temperature and VPD affect WUE, so that the higher the air temperature and VPD, the lower the WUE. Furthermore, it is observed that under lower air temperature and VPD (< 28°C and < 10 hPa, respectively), NEP increases strongly with a small increase in ET. On the other hand, an opposite pattern is observed when the air temperature exceeds 32°C and the VPD overcomes the 20 hPa since the plant needs to evapotranspire more so that the assimilation increases a bit.

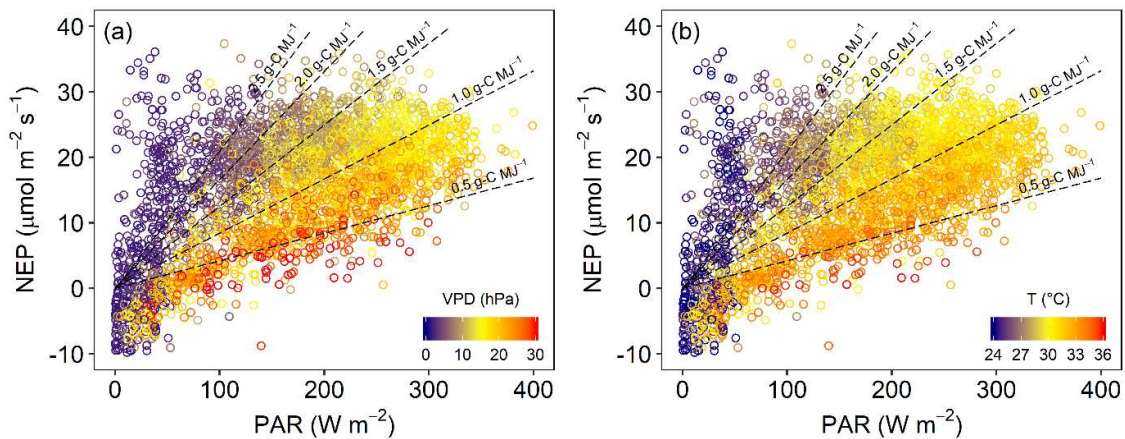
Figure 14 – Decomposition of WUE into NEP and ET components. Iso-efficiency is shown by black dashed lines with their respective values of WUE. Circle colors present the VPD (a) and air temperature (b)



Source: Author.

LUE was also sensitive to the variation in air temperature and VPD. Figure 15 shows that for low PAR ($< 150 \text{ W m}^{-2}$), carbon assimilation was often less than the ecosystem respiration, making NEP less than zero, even under air temperature and VPD close to ideal conditions. Under high air temperature ($> 34^\circ\text{C}$) and high VPD ($> 20 \text{ hPa}$), LUE was not limited by radiation, so that the low efficiency was due to the reduced NEP caused by unfavorable air temperature and VPD conditions. The LUE was higher for moderate air temperature ($< 30^\circ\text{C}$) and VPD ($< 20 \text{ hPa}$), but it was limited by light saturation, where NEP does not exceed $30 \mu\text{mol m}^{-2} \text{ s}^{-1}$. However, even under light saturation conditions, the LUE was sensitive to air temperature and VPD, since the NEP reduced steadily with rising of both VPD and air temperature (rate of $-0.5 \mu\text{mol-CO}_2 \text{ m}^{-2} \text{ s}^{-1} \text{ hPa}^{-1}$ and $-0.14 \mu\text{mol-CO}_2 \text{ m}^{-2} \text{ s}^{-1} \text{ }^\circ\text{C}^{-1}$, respectively).

Figure 15 – Decomposition of LUE into NEP and PAR components. Iso-efficiency is shown by black dashed lines with their respective values of LUE. Circle colors present the VPD (a) and air temperature (b)



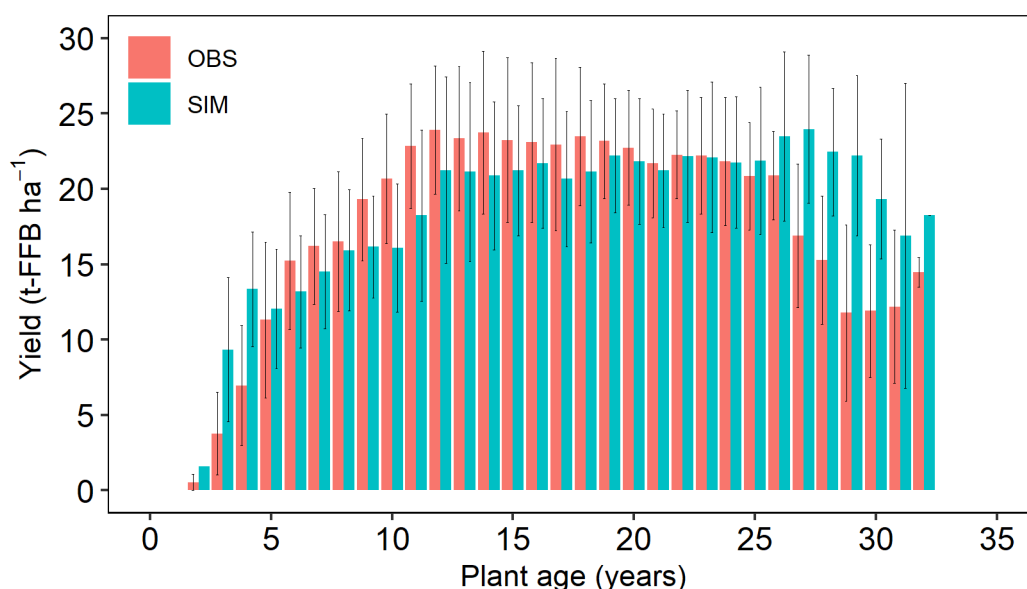
Source: Author.

3.3. Yield simulations

The long-term average annual yield of all studied farms was $18.39 \pm 7.33 \text{ t-FFB ha}^{-1}$ (tons of fresh fruit bunches per hectare) during the study period, but this yield was not constant throughout the whole life plantation. On average, oil palm yield increases steadily from 2~3 YPP (years past planting) to 10~12 YPP, reaching an average yield of $\sim 20.0 \text{ t-FFB ha}^{-1}$. From then on, the yield becomes almost constant until 25 YPP, when it starts to decrease (Figure 16). The standard deviation bars in Figure 16 show that, although the yield varies a lot for plantation with the same age, the growth, stability and decrease stages have remained. The simulated long-term average of the yield was close to that observed ($17.84 \pm 6.14 \text{ t-FFB ha}^{-1}$), with an RB

of -2.98%. However, although the yield behavior related to planting age was well simulated by the model, mainly for the stable yield stage (≥ 12 YPP, $RB = -6.1\%$), in the first harvests (≤ 5 YPP, $RB = 49.0\%$) and in very old plantation (> 25 YPP, $RB = 39.0\%$), the simulated yield was largely overestimated. Last, during the growing yield stage (> 5 YPP), the model underestimated the observed yield ($RB = -14.1\%$). It is important to note that the drop in yield observed after 25 YPP is due to a management issue. The plants become very tall, making harvesting difficult and some fruit bunches are not harvested. Thus, the reduction observed after 25 YPP may not represent a real drop in crop yield, so it is not possible to say that the model overestimates yield in older plants.

Figure 16 – Oil palm average yield according to the plantation age. Light red and blue bars are the observed and simulated monthly yield, and the vertical lines are the standard deviation

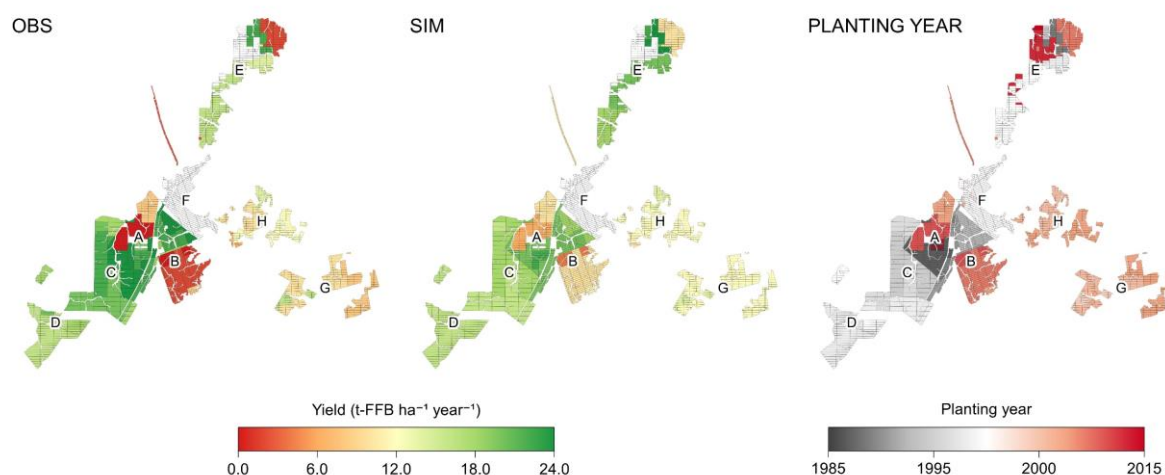


Source: Author.

The annual yield of oil palm plantations also varied among the farms (Figure 17). Farms A and C achieved the highest long-term annual mean yield (20.45 t-FFB ha⁻¹ and 22.84 t-FFB ha⁻¹, respectively), while the lowest yield was achieved by farms G and H (12.24 t-FFB ha⁻¹ and 12.12 t-FFB ha⁻¹, respectively). The average yield on farms B (18.21 t-FFB ha⁻¹), D (18.85 t-FFB ha⁻¹), and E (16.80 t-FFB ha⁻¹) was similar to the general average yield for all farms. The model simulated the yield of farms A, B, and G with good accuracy, with RB of 1.96%, -1.45%, and -3.50%, respectively. For farms C and E, the model performance to simulate the yield was quite lower than that achieved by farms A, B, and G, with RB of 19.70% and -18.76%, respectively. For farms D and G, the model performed a slightly better simulation than that achieved for farms C and E, with RB of 12.96% and -14.30%,

respectively. Note that the yield of plot groups is highly correlated with the planting age, so that younger plot groups presented a reduced yield, in addition to worse simulation performance.

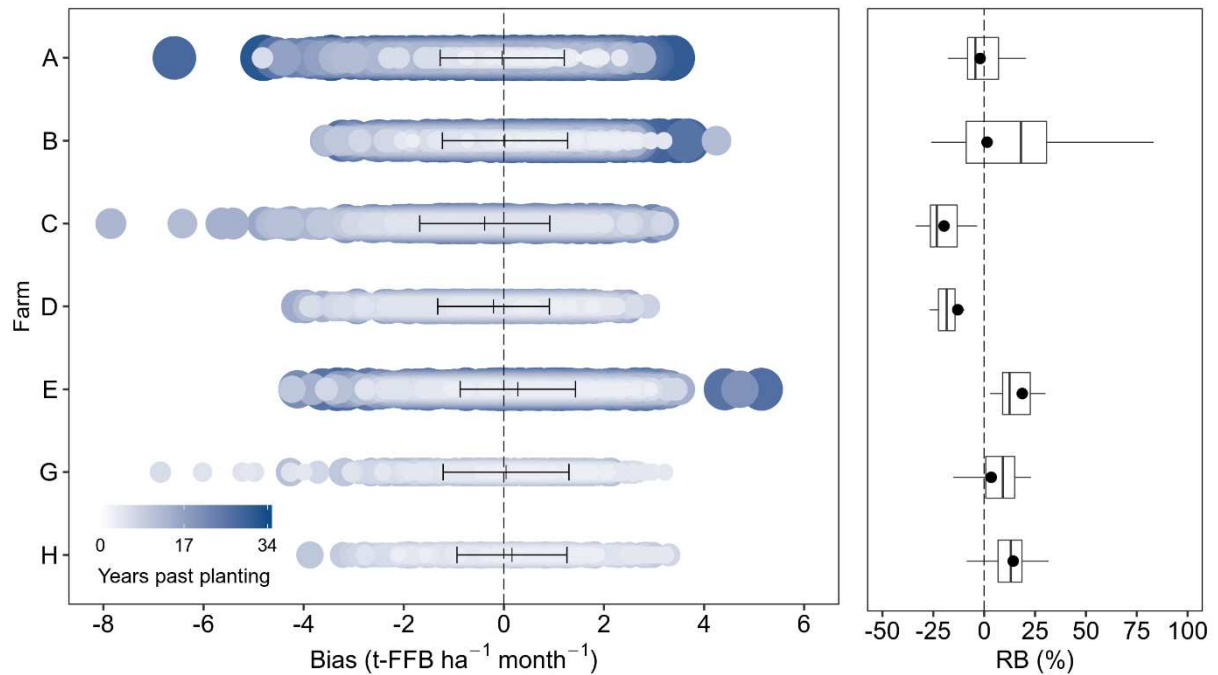
Figure 17 – Observed (OBS), simulated (SIM) mean of annual yield, and the planting year for each plot groups. The letters A to H are the centroid of the farms. There is no available dataset for farm F



Source: Author.

Crop yield also varied widely on a monthly time scale across farm plot groups. The yield of plot groups on farm B proved to be the least homogeneous, with a CV of 38.3%. The yield range of plot groups on farms A and E was also large, with a CV of 28.0% and 20.1%, respectively. For farms G and H, the variation in yield among plot groups was slightly lower, with CV of 17.3% and 13.5%, respectively. Finally, the variation in yield among plot groups on farms C and D was much lower than the others, with CV of 6.7% and 6.2%, respectively. This variation in yield among plot groups planted in the same farm could be explained by the range of plot planting year. Farms with plots planted in a small interval of years show a more homogeneous yield than farms with plots planted over the study period. For example, on farm B there are plots planted since the mid-1980s, through the 1990s, and also in the early 2010s. On the other hand, plots on farms C and D were planted between the second half of the 1990s to the beginning of the 2000s. The variation in the planting year also affects the model performance to simulate the average yield of the farms due to an offsetting error effect. Thus, farms with plots planted over a wide range of years have a lower average error, since the performance of the model is affected by the age of the plot. The left-hand chart in Figure 18 shows the bias (difference between observed simulated values) of the yield of all plot groups of per farm. Note that the yield of the older plot groups (circles in dark blue tones) has the largest errors.

Figure 18 – Monthly yield bias distribution for each farm (left-hand chart). Bars show the median \pm standard deviation. The color of the circles is the plant age when the yield was simulated. Boxplot in the right-side frame present the distribution of the RB of the plot groups in the farms, so that the box includes 50% of the data, with the horizontal tick inside the box as the median. Black dots represent the mean RB of each farm

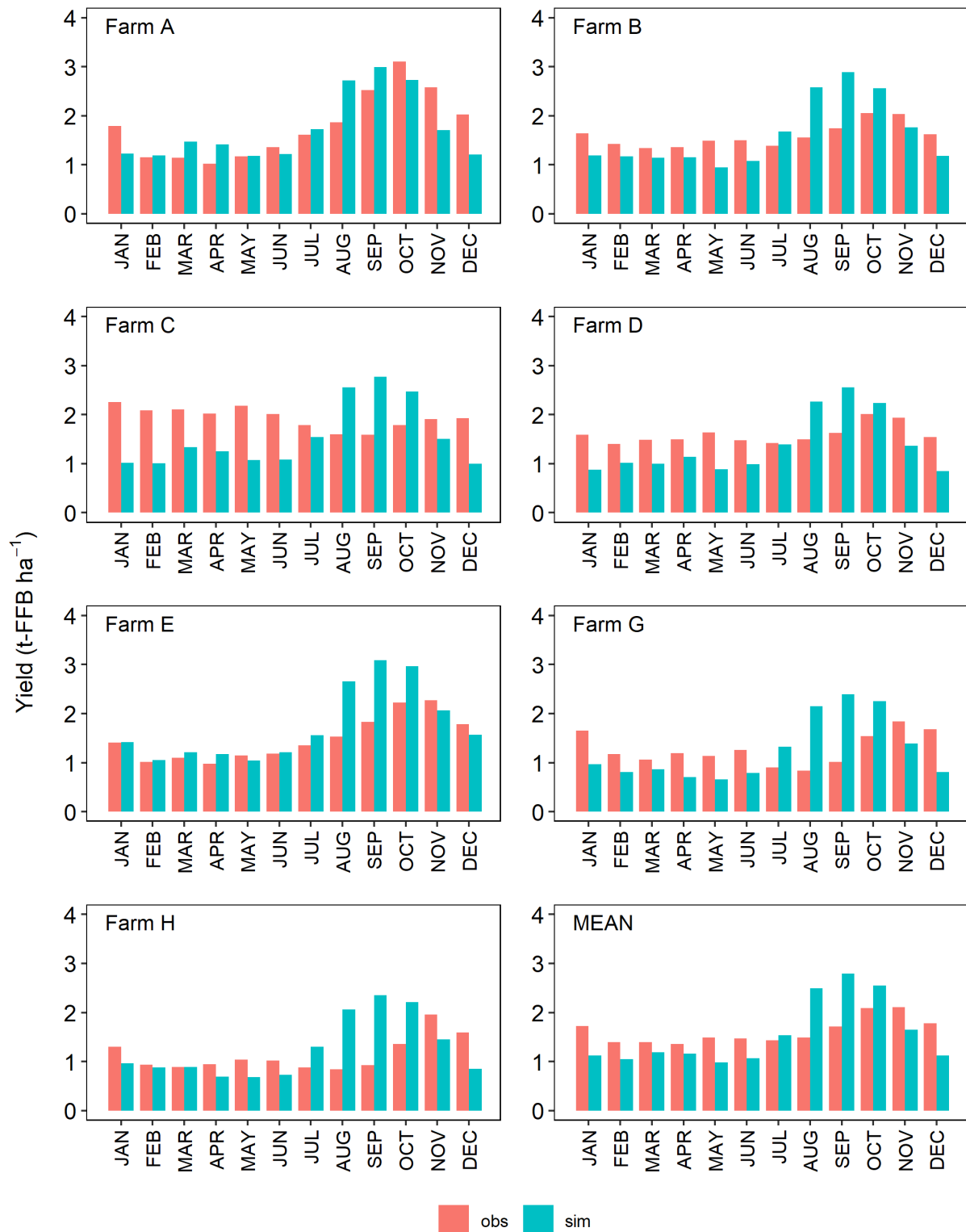


Source: Author

Oil palm yields also varied on a monthly time scale (MEAN, Figure 19). From February to August, the yield was similar for all months (~ 1.5 t-FFB ha⁻¹). From September onwards, yields begin to rise, peaking in October and November (~ 2.1 t-FFB ha⁻¹), and then reduces. The monthly behavior of the simulated yield also varied, but with greater amplitude and with the high-yield period beginning two months earlier. From December to June, the yield was almost constant, ranging between 1.3 t-FFB ha⁻¹ and 1.5 t-FFB ha⁻¹. From July onwards, the yield begins to rise, peaking in September (2.8 t-FFB ha⁻¹), and then reduces. We also observed a large variation in the monthly yield among farms (farms from A to H, Figure 19). Strong seasonality was observed in the plot groups yield on farms A and E. Yield from farms B, G, and H showed a slight seasonality, whereas farms C and D produce almost in the same level throughout the months. Farms A, B, and E reached the largest yield between September and December, whereas the yield from farms G and H was highest from October to January.

Despite the low seasonality, the yield of farm D slightly increase in October and November, and farm C produces a bit more from January to June (Figure 19).

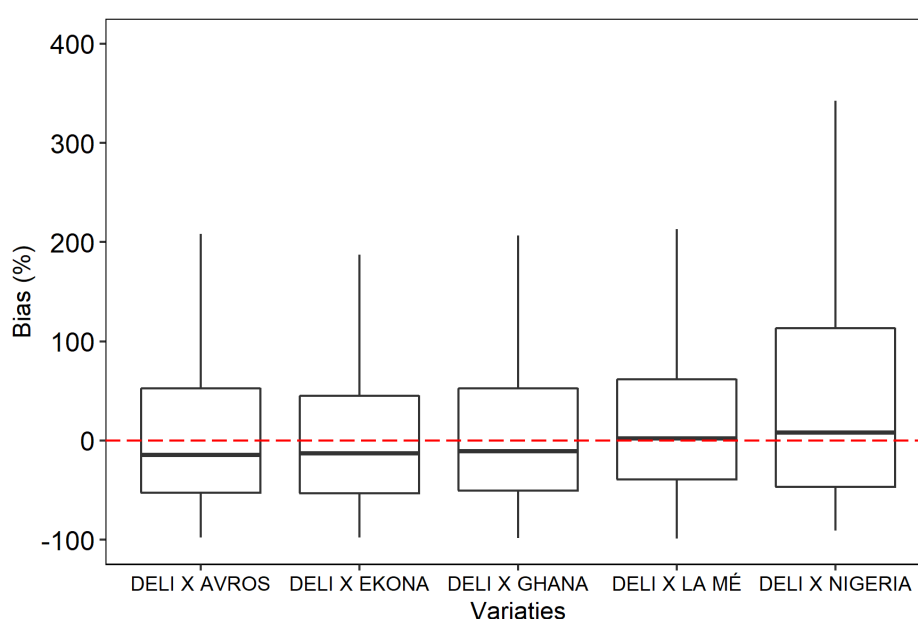
Figure 19 – Yield monthly mean for farms A, B, C, D, E, G, H, and the general mean (MEAN) of farms. Light red bars present the observed yield data and blue bars present the simulated yield



Source: Author.

In addition to the climate, the genetic factor also affects the seasonal yield of the oil palm crop. This study was limited to the calibration of the model to carbon and energy fluxes. However, there are genetic factors that cause variation in crop yield, in addition to the dynamics of NPP (Barcelos *et al.*, 2015). Figure 20 shows the percentage bias between the simulated and observed yield of the varieties that cover at least 5% of the total area of the studied farms. We observed that, on average, the model underestimated the yield for the Deli x Avros, Deli x Ekona, and Deli x Ghana varieties, whereas the yield of the Deli x La Mé and Deli x Nigeria varieties is overestimated. Furthermore, it is noted that the model presented the best performance to simulate the Deli x La Mé variety, with an average bias of 1.83%. For the other varieties, the average bias was -10.87% for Deli x Ghana, -13.12% for Deli x Ekona, -14.54% for Deli x Avros, and 16.26% for Deli x Nigeria.

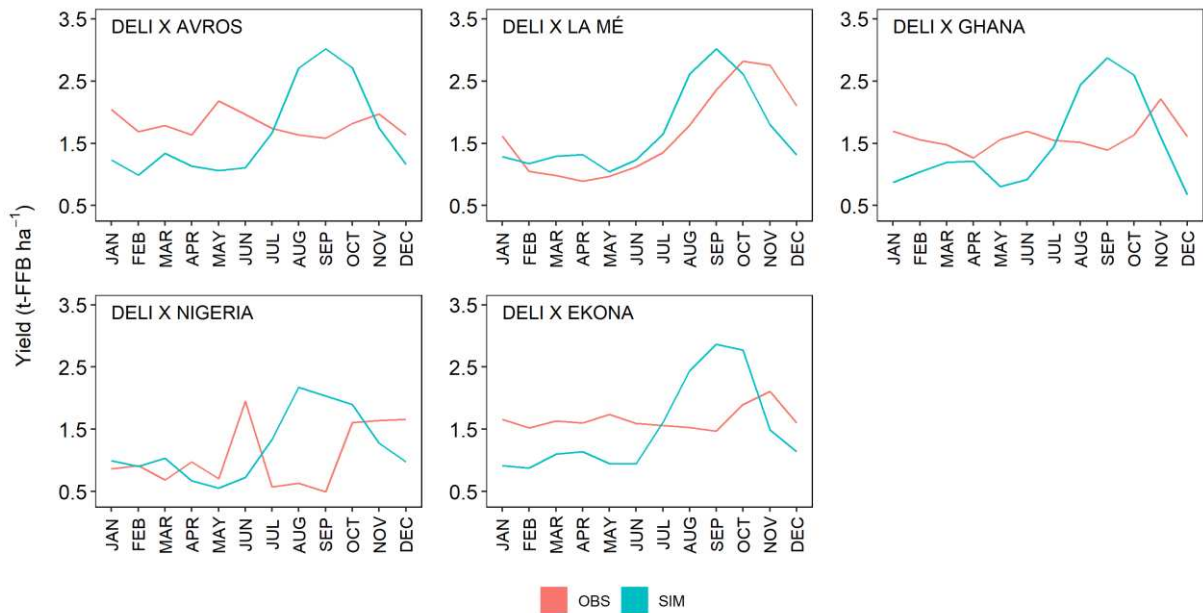
Figure 20 – Average percentage bias for the main varieties planted on the studied farms.



Source: Author.

It should also be noted that the variety Deli x La Mé showed the highest seasonality in yield. The average amplitude (average of the difference between the months with the highest and lowest yield) of the observed variety yield was 5.43 t-FFB ha⁻¹, whereas in the other varieties the average amplitude was less than 4.5 t-FFB ha⁻¹ (Figure 21). Seasonality in the varieties yield could be also seen in the farms monthly yield (see Figure 19), since there are different predominant varieties in each farm. On farm A, for example, more than 50% of the plots are planted with the high-seasonality variety Deli x La Mé, whereas on farm C, prevails the low-seasonality varieties Deli x Ekona (23%) and Deli x Ghana (20%). Therefore, varieties with marked seasonal yield are generally best simulated by the model.

Figure 21 – Seasonal yield behavior of the five most planted varieties in the study area. Deli x La Mé is the most planted variety in the study area (27%), followed by Deli x Ghana (14%), Deli x Ekona (12%), Deli x Avros (10%), and Deli x Nigeria (9.5%). Light red and blue lines present the observed and simulated monthly mean yield, respectively



Source: Author.

4. DISCUSSION

4.1. Climate dependence on oil palm carbon uptake efficiency

Previous studies have shown that oil palm achieve a high rate of photosynthesis compared to others C_3 photosynthesis pathway plants, saturating at a PPFD (Photosynthetic Photon Fluence Density) of $1,100 \mu\text{mol m}^{-2} \text{s}^{-1}$ ($\sim 240 \text{ W m}^{-2}$ of PAR) in $\sim 20 \mu\text{mol-CO}_2 \text{ m}^{-2} \text{s}^{-1}$ (Apichatmeta, Sudsiri and Ritchie, 2017; Dufrene and Saugier, 1993). Also, the palm oil growth is satisfied with PAR of at least $230 \text{ MJ m}^{-2} \text{month}^{-1}$ (Woittiez *et al.*, 2017), which is commonly overcome in the equatorial region, where MOJ site is located. On the other hand, the water demand by the oil palm is high, estimated at $\sim 6 \text{ mm day}^{-1}$ under non-limiting conditions (Woittiez *et al.*, 2017). This high demand is probably due to its equatorial origin, where rainfall is abundant throughout the year. Water stress affects the plantation severely, causing vegetative disturbances, such as accumulation of unopened leaves, premature senescence of the older leaves, and abortion of fruit bunches, leading the plant to death in severe cases (Caliman and Southworth, 1998). In order to avoid excessive water loss under dry conditions, the plant has a strong control over the stomatal opening, which controls the exchange of gases between the intracellular medium and the underlying atmosphere (Lamade and Bouillet, 2005).

Due to the strong stomatal control, environmental factors such as VPD, strongly affect the leaves carbon uptake and assimilation. Under high-VPD conditions, the plant reduces the rate of CO_2 uptake due to stomatal closure, also affecting the NEP, since less CO_2 is available for photosynthesis in the leaf intracellular medium. In addition, air temperature also affects NEP, so that under warmer conditions ($T > 34^\circ\text{C}$), the leaves could overheat, inhibiting photosynthesis, at the same time that promotes carbon loss due to increased ecosystem respiration. On the other hand, under very temperatures ($T < 12^\circ\text{C}$), vegetative development and fruit ripening are slower than normal. (Corley and Tinker, 2015; Lamade and Bouillet, 2005). It is not expected that in equatorial regions the oil palm will experience excessively low air temperatures events, but it is common that in some periods of the day the higher air temperature causes thermal stress. Indeed, extreme warm events ($T > 34^\circ\text{C}$) were recorded on the MOJ site in 2015, mainly in October and November, where the frequency of occurrence was 8.3% and 14.1%, respectively.

The results showed that the WUE and LUE is strongly dependent of the variation in carbon assimilation, so that under less favorable climate conditions, especially under excessively warm and high-VPD conditions, the WUE and LUE are reduced due to the lower carbon assimilation rate (Dufrene and Saugier, 1993; Lamade and Bouillet, 2005; Niu *et al.*,

2015; Smith, 1989). The reduction in the assimilation of carbon by the plant lead to a reduction in the yield of the crop since the yield of the oil palm is limited by the source (Legros, Mialet-Serra, Clement-Vidal, *et al.*, 2009). Therefore, the results show that the expected climate changes for eastern Amazonia can strongly affect Brazilian oil palm production, but they also present ways to offset the negative effects of climate change. Through the management of plant density and water availability in the soil, the drop in WUE and LUE can be compensated for, reducing the loss of carbon assimilation due to the future warmer and drier climate.

It is noteworthy that the WUE and LUE were estimated based on the NEP. Thus, the variation in net carbon assimilation can have two possible explanations: (i) the NEP depends on the rate of photosynthesis, which varies depending on the VPD and the air temperature; or (ii) NEP varies due to the variation in ecosystem respiration, which is affected by air temperature. Indeed, both effects are likely to affect the variation of NEP, but it was not possible to identify which effect prevails with the data available in this study.

4.2. Modelling the oil palm growing and yield

The model described in this study considered only NPP as a limiting factor for crop yield. Indeed, Fan *et al.* (2015) showed that the crop yield source-limited equation was able to capture the yield dynamics under optimal and stress conditions, so that under stress conditions (e.g. water limitation), NPP is reduced, limiting yield. Models based on land surface processes, such as ECOSMOS, are usually better to simulate the dry matter assimilation dynamics because they consider the complete carbon cycle in the plant. Processes such as respiration and photosynthesis are simulated explicitly and consider water availability in the soil, radiation, air temperature and the vapor pressure deficit in the assimilation of carbon. Other models that simulate oil palm yield, such as PALMSIM (Hoffmann *et al.*, 2014) and ECOPALM (Combres *et al.*, 2013) are more limited to simulate the plant carbon dynamics, since they are mainly limited by radiation.

Previous studies have shown that disturbances in the source of assimilates affected the yield of oil palm, so that the reduction in the amount of assimilates caused by pruning, for example, could reduce the yield (Jones, 1997; Legros, Mialet-Serra, Caliman, *et al.*, 2009; Legros, Mialet-Serra, Clement-Vidal, *et al.*, 2009). However, it was observed that the crop yield in younger (<12 YPP) or older (>25 YPP) plants was lower compared to plants aged between 5 YPP and 25 YPP. The yield of the oil palm changes with age, mainly due to the change in the

proportion of female inflorescences and the average weight of the mature bunches (Woittiez *et al.*, 2017). In this study, only the dynamics of the NPP was considered as a source of variation in the allocation rate of assimilates to the fruits, but factors such as the sex ratio and the rate of abortions of inflorescences or developing bunches affect the yield of the oil palm crop (Corley and Tinker, 2015). These factors vary not only according to the availability of assimilates, but also with the age of the plant (Jones, 1997; Woittiez *et al.*, 2017) and were not considered in the development of this model due to data limitations. However, even without considering these factors, the model still managed to capture with satisfactory accuracy the dynamics of crop yield as a function of plant age. It is also noteworthy that for plots with more than 25 YPP, the yield observed in the field also reduces due to the difficulty in harvesting the fruit bunches due to the size of the plants. Thus, the low performance of the model to simulate the yield in older plants may have been caused by the inaccuracy of the observed data.

The genetic factor has also been shown to significantly affect oil palm yield, mainly in seasonality. Some varieties showed a more seasonal yield, while others show a more homogeneous yield throughout the year. This result shows that a high genetic variability is desirable in a commercial plantation, in order to maintain the yield at higher levels throughout the year. On farm A, for example, during the first half of the year the yield is much lower than farms grown with less seasonal varieties, such as C, despite the high yield in the second half of the year. In addition, the model was not able to consider genetic variability in the simulation of crop yield, so that only the most seasonal varieties were well simulated. This result suggest that the JAM site was probably cultivated with some seasonal variety when eddy covariance measurements were taken, affecting the calibration of the model parameters.

Despite the satisfactory result to simulate oil palm yield, the model developed in this study fails to answer some questions, such as the importance of reproductive factors in the dynamics of growth and crop yield. The lack of data about the plant's reproductive stage limited this study to consider only age as an explicit endogenous variation factor in the growth and yield of the crop. Further studies may improve the dry matter allocation equation for fruits considering not only the NPP in the carbon allocation dynamics for the fruits, but also factors such as the sex ratio and the rate of inflorescences and developing bunches. In addition, a robust multi-variety calibration is necessary for the model to be able to capture the variation in yield between the main genetic materials used by producers.

4.3. Study limitations

The results found in this study point to a good performance of the model, but some considerations must be made about the limitations of this study. The main limitations of this study are related to data availability and quality. First, it was observed that the model is sensitive to the physical characteristics of the soil. Soil physics characteristics control processes such as the soil water content and soil heat transfer. Thus, the generic information used in this study inserts a great uncertainty in the results, mainly in the simulation of H, as presented in section 3.2. The soil data used in this study come from a global database, which includes few and not validated information about the soil properties. Also, important information, such as the permanent wilt point, field capacity, porosity and saturated hydraulic conductivity were estimated from this database applied to equations that were also not adjusted for this specific study site. It is expected that the inclusion of local soil properties will improve the model's results, mainly the H and LE simulations.

In addition to improving soil properties in the model, implementing equations for the oil palm reproductive cycle could also help improve the model's performance. As discussed in section 4.2, some characteristics of the oil palm reproductive cycle, such as sex ratio and developing bunch abortion rate, can greatly affect crop yield. It is also worth mentioning that another important limitation of the study was the lack of a robust calibration for genetic varieties. Multi-variate calibration is fundamental to improve the model's performance in simulating the yield on a monthly scale, since it was observed that each variety presents a different seasonal yield behavior of the crop. This improvement can assist farmers in choosing which variety to plant, according to their needs.

5. CONCLUSIONS

In this study the yield of oil palm in Brazil from a climatic perspective was analyzed. It is observed that the assimilation of carbon by the oil palm is strongly affected by climatic factors, such as air temperature and vapor pressure deficit. This climate-dependence makes efficiency in the use of some resources, such as solar radiation and water, also affected by these climatic factors, even when these resources are not scarce. It was also observed that the climate affects the yield of the oil palm, since the filling of the fruit bunches is also affected by the assimilates availability.

The model developed in this study proved to be able of simulating carbon and energy exchanges between the land surface and the atmosphere on an hourly time scale. The exception was the simulation of the sensitive heat flux, which was affected by the lack of data on the soil physical properties. In addition, the model was also able to simulate well the oil palm yield in the main producing region of Brazil. In general, the model better simulated the yield of plants from 12 to 25 years old and for varieties that showed higher seasonality in yield, while the yield in younger (<5 YPP) or older plants (> 25 YPP) was overestimated .

Despite showing a good result, some improvements are required so that the model can simulate oil palm yield in more comprehensive conditions. One of the possible improvements that should be made is the multi-variety calibration, since only species with largely seasonal yield have been well simulated. In addition, the quality of the simulation proved to be dependent on soil properties, so that the inclusion of these information measured in the field can contribute to the improvement of the model.

Future studies should be conducted to include the simulation of the oil palm reproductive cycle in the model in order to improve the simulation of crop yield. In addition, it is essential that a multi-variety calibration is conducted in future studies, in order to make the model more general so that palm and oil producers can use the model in making decisions about which varieties should be planted.

6. REFERENCES

- ADAM, H.; JOUANNIC, S.; ESCOUTE, J.; DUVAL, Y.; VERDEIL, J.-L.; TREGGAR, J. W. **Reproductive developmental complexity in the African oil palm (*Elaeis guineensis*, *Arecaceae*)**. American Journal of Botany, v. 92, n. 11, p. 1836–1852, 2005.
- ALMEIDA, C. T.; OLIVEIRA-JÚNIOR, J. F.; DELGADO, R. C.; CUBO, P.; RAMOS, M. C. **Spatiotemporal rainfall and temperature trends throughout the Brazilian Legal Amazon, 1973-2013**. International Journal of Climatology, v. 37, n. 4, p. 2013–2026, 2017.
- APICCHATMETA, K.; SUDSIRI, C. J.; RITCHIE, R. J. **Photosynthesis of Oil Palm (*Elaeis guineensis*)**. Scientia Horticulturae, v. 214, p. 34–40, 2017.
- AVILA-DIAZ, A.; BENEZOLI, V.; JUSTINO, F.; TORRES, R.; WILSON, A. **Assessing current and future trends of climate extremes across Brazil based on reanalyses and earth system model projections**. Climate Dynamics, v. 55, n. 5–6, p. 1403–1426, 2020.
- BARCELOS, E.; RIOS, S. DE A.; CUNHA, R. N. V.; LOPES, R.; MOTOIKE, S. Y.; BABIYCHUK, E.; SKIRYCZ, A.; KUSHNIR, S. **Oil palm natural diversity and the potential for yield improvement**. Frontiers in Plant Science, v. 6, n. MAR, p. 1–16, 2015.
- BARR, A. G. *et al.* **Use of change-point detection for friction–velocity threshold evaluation in eddy-covariance studies**. Agricultural and Forest Meteorology, v. 171–172, p. 31–45, 2013.
- BREURE, C. J. **Development of Leaves in Oil Palm (*Elaeis Guineensis*) and Determination of Leaf Opening Rate**. Experimental Agriculture, v. 30, n. 04, p. 467, 1994.
- C3S, C. C. C. S. **ERA5: Fifth generation of ECMWF atmospheric reanalyses of the global climate**. Disponível em: <<https://cds.climate.copernicus.eu/cdsapp#!/home>>.
- CALIMAN, J. P.; SOUTHWORTH, A. **Effect of drought and haze on the performance of oil palm** International Oil Palm Conference. Anais...Bali: 1998 Disponível em: <<http://agritrop.cirad.fr/401034/1/ID401034.pdf>>. Acesso em: 23 apr. 2018
- CHEN, N.; ZHU, J.; ZHANG, Y.; LIU, Y.; LI, J.; ZU, J.; HUANG, K. **Nonlinear response of ecosystem respiration to multiple levels of temperature increases**. Ecology and Evolution, v. 9, n. 3, p. 925–937, 2019.
- CLAPP, R. B.; HORNBERGER, G. M. **Empirical equations for some soil hydraulic properties**. Water Resources Research, v. 14, n. 4, p. 601–604, 1978.
- COLLATZ, G. J.; BALL, J. T.; GRIVET, C.; BERRY, J. A. **Physiological and environmental regulation of stomatal conductance, photosynthesis and transpiration: a model that includes a laminar boundary layer**. Agricultural and Forest Meteorology, v. 54, n. 2–4, p. 107–136, 1991.
- COMBRES, J.-C.; PALLAS, B.; ROUAN, L.; MIALET-SERRA, I.; CALIMAN, J.-P.; BRACONNIER, S.; SOULIÉ, J.-C.; DINGKUHN, M. **Simulation of inflorescence dynamics in oil palm and estimation of environment-sensitive phenological phases: a model based analysis**. Functional Plant Biology, v. 40, n. 3, p. 263, 2013.

CORLEY, R. H. V.; TINKER, P. B. **The Oil Palm**. Chichester, UK: John Wiley & Sons, Ltd, 2015.

COSBY, B. J.; HORNBERGER, G. M.; CLAPP, R. B.; GINN, T. R. **A Statistical Exploration of the Relationships of Soil Moisture Characteristics to the Physical Properties of Soils**. Water Resources Research, v. 20, n. 6, p. 682–690, 1984.

DUFRENE, E.; SAUGIER, B. **Gas Exchange of Oil Palm in Relation to Light, Vapour Pressure Deficit, Temperature and Leaf Age**. Functional Ecology, v. 7, n. 1, p. 97, 1993.

FAN, Y.; ROUPSARD, O.; BERNOUX, M.; MAIRE, G. LE; PANFEROV, O.; KOTOWSKA, M. M.; KNOHL, A. **A sub-canopy structure for simulating oil palm in the Community Land Model (CLM-Palm): phenology, allocation and yield**. Geosci. Model Dev, v. 8, p. 3785–3800, 2015.

FARQUHAR, G. D.; CAEMMERER, S. VON; BERRY, J. A. **A biochemical model of photosynthetic CO₂ assimilation in leaves of C₃ species**. Planta, v. 149, n. 1, p. 78–90, 1980.

FEROLDI, M.; CREMONEZ, P. A.; ESTEVAM, A. **Dendê: do cultivo da palma à produção de biodiesel**. Revista Monografias Ambientais, v. 13, n. 5, p. 3800–3808, 2014.

FOLEY, J. A.; PRENTICE, I. C.; RAMANKUTTY, N.; LEVIS, S.; POLLARD, D.; SITCH, S.; HAXELTINE, A. **An integrated biosphere model of land surface processes, terrestrial carbon balance, and vegetation dynamics**. Global Biogeochemical Cycles, v. 10, n. 4, p. 603–628, 1996.

FONSECA, L. C. N. DA; ARAÚJO, A. C. DE; MANZI, A. O.; CARVALHO, C. J. R. DE; OLIVEIRA, L. R. DE. **Fluxos de CO₂ em Plantio de Palma de Óleo no Leste da Amazônia**. Revista Brasileira de Meteorologia, v. 33, n. 1, p. 181–192, 2018.

FORERO, D. C.; HORMAZA, P.; ROMERO, H. M. **Phenological growth stages of African oil palm (*Elaeis guineensis*)**. Annals of Applied Biology, v. 160, n. 1, p. 56–65, 2012.

FURUMO, P. R.; AIDE, T. M. **Characterizing commercial oil palm expansion in Latin America: land use change and trade**. Environmental Research Letters, v. 12, n. 2, p. 024008, 2017.

HAYATI, A.; WICKNESWARI, R.; MAIZURA, I.; RAJANAIDU, N. **Genetic diversity of oil palm (*Elaeis guineensis* Jacq.) germplasm collections from Africa: implications for improvement and conservation of genetic resources**. TAG Theoretical and Applied Genetics, v. 108, n. 7, p. 1274–1284, 2004.

HENGL, T. *et al.* **SoilGrids250m: Global gridded soil information based on machine learning**. PLoS ONE, v. 12, n. 2, p. e0169748, 2017.

HOFFMANN, M. P. *et al.* **Yield gap analysis in oil palm: Framework development and application in commercial operations in Southeast Asia**. Agricultural Systems, v. 151, p. 12–19, 2017.

HOFFMANN, M. P.; CASTANEDA VERA, A.; WIJK, M. T. VAN; GILLER, K. E.; OBERTHÜR, T.; DONOUGH, C.; WHITBREAD, A. M. **Simulating potential growth and**

yield of oil palm (*Elaeis guineensis*) with PALMSIM: Model description, evaluation and application. *Agricultural Systems*, v. 131, p. 1–10, 2014.

HUTH, N. I.; BANABAS, M.; NELSON, P. N.; WEBB, M. **Development of an oil palm cropping systems model: Lessons learned and future directions.** *Environmental Modelling & Software*, v. 62, p. 411–419, 2014.

JONES, L. H. **The Effects of Leaf Pruning and other Stresses on Sex Determination in the Oil Palm and their Representation by a Computer Simulation.** *Journal of Theoretical Biology*, v. 187, n. 2, p. 241–260, 1997.

KOTOWSKA, M. M.; LEUSCHNER, C.; TRIADIATI, T.; MERIEM, S.; HERTEL, D. **Quantifying above- and belowground biomass carbon loss with forest conversion in tropical lowlands of Sumatra (Indonesia).** *Global Change Biology*, v. 21, n. 10, p. 3620–3634, 2015.

KUCHARIK, C. J.; BRYE, K. R. **Integrated Biosphere Simulator (IBIS) Yield and Nitrate Loss Predictions for Wisconsin Maize Receiving Varied Amounts of Nitrogen Fertilizer.** *Journal of Environmental Quality*, v. 32, n. 1, p. 247–268, 2003.

LAMADE, E.; BOUILLET, J.-P. **Carbon storage and global change: the role of oil palm.** *Oléagineux, Corps gras, Lipides*, v. 12, n. 2, p. 154–160, 2005.

LEGROS, S.; MIALET-SERRA, I.; CALIMAN, J.-P.; SIREGAR, F. A.; CLEMENT-VIDAL, A.; FABRE, D.; DINGKUHN, M. **Phenology, growth and physiological adjustments of oil palm (*Elaeis guineensis*) to sink limitation induced by fruit pruning.** *Annals of Botany*, v. 104, n. 6, p. 1183–1194, 2009.

LEGROS, S.; MIALET-SERRA, I.; CLEMENT-VIDAL, A.; CALIMAN, J.-P.; SIREGAR, F. A.; FABRE, D.; DINGKUHN, M. **Role of transitory carbon reserves during adjustment to climate variability and source-sink imbalances in oil palm (*Elaeis guineensis*).** *Tree Physiology*, v. 29, n. 10, p. 1199–1211, 2009.

LEUNING, R. **A critical appraisal of a combined stomatal-photosynthesis model for C3 plants.** *Plant, Cell & Environment*, v. 18, n. 4, p. 339–355, 1995.

MAIZURA, I.; RAJANAIDU, N.; ZAKRI, A. H.; CHEAH, S. C. **Assessment of Genetic Diversity in Oil Palm (*Elaeis guineensis* Jacq.) using Restriction Fragment Length Polymorphism (RFLP).** *Genetic Resources and Crop Evolution*, v. 53, n. 1, p. 187–195, 2006.

MAUDER, M.; FOKEN, T. **Impact of post-field data processing on eddy covariance flux estimates and energy balance closure.** *Meteorologische Zeitschrift*, v. 15, n. 6, p. 597–609, 2006.

MEIJIDE, A.; RÖLL, A.; FAN, Y.; HERBST, M.; NIU, F.; TIEDEMANN, F.; JUNE, T.; RAUF, A.; HÖLSCHER, D.; KNOHL, A. **Controls of water and energy fluxes in oil palm plantations: Environmental variables and oil palm age.** *Agricultural and Forest Meteorology*, 2017.

NIU, F.; ROLL, A.; HARDANTO, A.; MEIJIDE, A.; KOHLER, M.; HENDRAYANTO; HOLSCHER, D. **Oil palm water use: calibration of a sap flux method and a field**

measurement scheme. *Tree Physiology*, v. 35, n. 5, p. 563–573, 2015.

PATERSON, R. R. M.; KUMAR, L.; SHABANI, F.; LIMA, N. **World climate suitability projections to 2050 and 2100 for growing oil palm.** *Journal of Agricultural Science*, v. 155, n. 5, p. 659–702, 2017.

PIRKER, J.; MOSNIER, A.; KRAXNER, F.; HAVLÍK, P.; OBERSTEINER, M. **What are the limits to oil palm expansion?** *Global Environmental Change*, v. 40, p. 73–81, 2016.

SAGE, R. F.; KUBIEN, D. S. **The temperature response of C 3 and C 4 photosynthesis.** *Plant, Cell & Environment*, v. 30, n. 9, p. 1086–1106, 2007.

SELLERS, P. J. **Modeling the Exchanges of Energy, Water, and Carbon Between Continents and the Atmosphere.** *Science*, v. 275, n. 5299, p. 502–509, 1997.

SILVA, P. E. DA; SANTOS E SILVA, C. M.; SPYRIDES, M. H. C.; ANDRADE, L. DE M. B. **Precipitation and air temperature extremes in the Amazon and northeast Brazil.** *International Journal of Climatology*, v. 39, n. 2, p. 579–595, 2019.

SMITH, B. G. **The Effects of Soil Water and Atmospheric Vapour Pressure Deficit on Stomatal Behaviour and Photosynthesis in the Oil Palm.** *Journal of Experimental Botany*, v. 40, n. 6, p. 647–651, 1989.

SPARKS, A. **nasapower: A NASA POWER Global Meteorology, Surface Solar Energy and Climatology Data Client for R.** *Journal of Open Source Software*, v. 3, n. 30, p. 1035, 2018.

STIEGLER, C.; MEIJIDE, A.; FAN, Y.; ASHWEEN ALI, A.; JUNE, T.; KNOHL, A. **El Niño–Southern Oscillation (ENSO) event reduces CO2 uptake of an Indonesian oil palm plantation.** *Biogeosciences Discussions*, v. 16, n. 14, p. 1–27, 2019.

VIJAY, V.; PIMM, S. L.; JENKINS, C. N.; SMITH, S. J. **The Impacts of Oil Palm on Recent Deforestation and Biodiversity Loss.** *PloS one*, 2016.

WEN, X. F.; YU, G. R.; SUN, X. M.; LI, Q. K.; LIU, Y. F.; ZHANG, L. M.; REN, C. Y.; FU, Y. L.; LI, Z. Q. **Soil moisture effect on the temperature dependence of ecosystem respiration in a subtropical Pinus plantation of southeastern China.** *Agricultural and Forest Meteorology*, v. 137, n. 3–4, p. 166–175, 2006.

WOITTIEZ, L. S.; WIJK, M. T. VAN; SLINGERLAND, M.; NOORDWIJK, M. VAN; GILLER, K. E. **Yield gaps in oil palm: A quantitative review of contributing factors.** *European Journal of Agronomy*, v. 83, p. 57–77, 2017.

XAVIER, A. C.; KING, C. W.; SCANLON, B. R. **Daily gridded meteorological variables in Brazil (1980–2013).** *International Journal of Climatology*, v. 36, n. 6, p. 2644–2659, 2016.

ZHANG, N.; WANG, Z. **Review of soil thermal conductivity and predictive models.** *International Journal of Thermal Sciences*, v. 117, p. 172–183, 2017.